AD-A256 721

②

NAVAL POSTGRADUATE SCHOOL
Monterey, California

THESIS

DYNAMIC RESPONSE AND FAILURE ANALYSIS OF
ALUMINUM CYLINDERS SUBJECTED TO
UNDERWATER EXPLOSION

by

Kurt W. Nelson

June, 1992

Advisor: Young S. Shin

Approved for public release; distribution is unlimited.

92-29048

6a. NAME OF PERFORMING ORGANIZATION Naval Postgraduate School	**6b. OFFICE SYMBOL** (If applicable) ME	**7a. NAME OF MONITORING ORGANIZATION** Naval Postgraduate School
6c. ADDRESS (City, State, and ZIP Code) Monterey, California 93943-5000		**7b. ADDRESS** (City, State, and ZIP Code) Monterey, California 93943-5000
8a. NAME OF FUNDING/SPONSORING ORGANIZATION	**8b. OFFICE SYMBOL** (If applicable)	**9. PROCUREMENT INSTRUMENT IDENTIFICATION NUMBER**

8c. ADDRESS (City, State, and ZIP Code)	**10. SOURCE OF FUNDING NUMBERS**			
	PROGRAM ELEMENT NO.	PROJECT NO.	TASK NO.	WORK UNIT ACCESSION NO.

11. TITLE (Include Security Classification)
DYNAMIC RESPONSE AND FAILURE ANALYSIS OF ALUMINUM CYLINDERS SUBJECTED TO UNDERWATER EXPLOSION

12. PERSONAL AUTHOR(S)
Nelson, Kurt W.

13a. TYPE OF REPORT Master's Thesis	**13b. TIME COVERED** FROM _____ TO _____	**14. DATE OF REPORT** (Yr., Mo., Day) 1992, June	**15. PAGE COUNT** 102

16. SUPPLEMENTARY NOTATION: The views expressed in this thesis are those of the author and do not reflect the official policy or position of the Department of Defense or the U.S. Government.

17. COSATI CODES			**18. SUBJECT TERMS** (Continue on reverse if necessary and identify by block number) Underwater shock
FIELD	GROUP	SUB-GROUP	

19. ABSTRACT (Continue on reverse if necessary and identify by block number)

An underwater explosion test was conducted on two closed aluminum cylinders to provide physical results from a dynamic collapse. Axial and side-on attack geometries were investigated in this study. Both cylinders displayed numerous fractures and significant plastic deformation. Finite element models of the cylinders were developed to aid in physical understanding of the dynamic response. Sensitivity analyses of the model parameters were conducted to determine the optimum modeling method. A computer model with failure prediction capability was utilized to investigate the dynamic failure mechanism.

20. DISTRIBUTION/AVAILABILITY OF ABSTRACT [XX] UNCLASSIFIED/UNLIMITED [ ] SAME AS RPT. [ ] DTIC USERS	**21. ABSTRACT SECURITY CLASSIFICATION** Unclassified
22a. NAME OF RESPONSIBLE INDIVIDUAL Young S. Shin	**22b. TELEPHONE** (Include Area Code) 408/646-2568 **22c. OFFICE SYMBOL** ME/Sg

DYNAMIC RESPONSE AND FAILURE ANALYSIS OF ALUMINUM CYLINDERS SUBJECTED TO UNDERWATER EXPLOSION

by

Kurt W. Nelson
Lieutenant Commander, United States Navy
B.S., Northwestern University, 1977

Submitted in partial fulfillment of the
requirements for the degree of
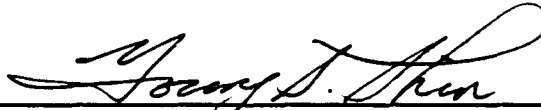
MASTER OF SCIENCE IN MECHANICAL ENGINEERING

from the

NAVAL POSTGRADUATE SCHOOL
June, 1992

Author: _____
Kurt W. Nelson

Approved by: _____
Young S. Shin, Thesis Advisor

_____
Young W. Kwon, Second Reader

_____
A.J. Healey, Chairman
Department of Mechanical Engineering

ii

ABSTRACT

An underwater explosion test was conducted on two closed aluminum cylinders to provide physical results from a dynamic collapse. Axial and side-on attack geometries were investigated in this study. Both cylinders displayed numerous fractures and significant plastic deformation. Finite element models of the cylinders were developed to aid in physical understanding of the dynamic response. Sensitivity analyses of the model parameters were conducted to determine the optimum modeling method. A computer model with failure prediction capability was utilized to investigate the dynamic failure mechanism.

DTIC QUALITY INSPECTED 4

Accesion For		
NTIS CRA&I		☒
DTIC TAB		☐
Unannounced		☐
Justification		
By		
Distribution /		
Availability Codes		
Dist	Avail and / or Special	
A-1		

TABLE OF CONTENTS

LIST OF FIGURES

I. INTRODUCTION

In the current economic climate, the need to provide better defense at a lower cost is essential. As the Navy begins to reduce the size of its fleet, individual ships will be required to perform a larger variety of missions. The high cost of producing new warships will cause even more emphasis to be placed on operating cycle maintenance.

A key element in ensuring our ships are ready to succeed in a variety of missions against an uncertain enemy is ship survivability. In particular, our ships must be able to maintain their combat capabilities after an enemy attack.

The underwater environment occupied by our submarines presents some unique problems with regard to ship survivability. The physics of an underwater explosion and the fluid-structure interaction represents a transient, nonlinear and very dynamic process which is only partially understood.

To help understand the physical phenomena of this interaction, much recent attention has been given to numerical solutions of the underwater shock problem. The rising cost of underwater explosion tests has been offset to some degree by the decrease in high speed computer costs and development of improved computer codes.

Present research at the Naval Postgraduate School in underwater shock effects includes a variety of topics to improve the physical understanding of these phenomena. The particular emphasis of this thesis is on the understanding of structural response due to shock-induced failures. The effect of a structural failure at a particular location was

seen to be strongly influenced by proximity to the failure zone. In addition, the location

of the failure zone was sensitive to geometric imperfections in the cylinder.

II. UNDERWATER EXPLOSION TEST AND ANALYSIS

An underwater explosion test was conducted at Dynamic Testing, Incorporated (DTI), in Rustburg, Virginia. The test facility consisted of a quarry filled with fresh water. The test was accomplished in an area with a total water depth of 130 feet which precluded bottom reflection interference with experimental results.

The test specimen was an instrumented aluminum cylinder. This cylinder was constructed of 6061-T6 aluminum with a diameter of 12 inches. The shell thickness was one-quarter inch. Flat aluminum endplates with a thickness of one inch were welded to the cylinder shell using the tungsten inert gas (TIG) process. The cylinder length was 42 inches and weight was approximately 60 pounds. Three padeyes were welded to each endplate to provide attachment points for cables and weights to achieve proper cylinder orientation during the test.

Instrumentation of the two cylinders consisted of CEA-series constantan strain gages with a strain limit of 50,000 microstrain. Instrumentation installation and data collection was performed by DTI technicians. A total of 20 strain gages were attached to the cylinder subjected to end-on attack as shown in Figure 1. The cylinder subjected to side-on attack was instrumented with 18 strain gages as shown in Figure 2. Gages were positioned to measure both axial and circumferential strains at these locations. The choice of gage locations was based on pre-test calculations to determine some critically

3

deformed zones. Three pressure transducers were used to measure free-field pressure. The compressive shock wave was provided by a 60 pound cylindrical charge of HBX-1.

The collection of strain gage and pressure response data was initially filtered at 50,000 Hertz to capture the peak pressure generated by the HBX-1 charge. To accurately represent the most significant modes of structural response (strains), this data was filtered at 2000 Hertz using a seventh-order Butterworth low-pass digital filter [Ref. 1]. This filter exhibits a flat magnitude response in the passband and stopband according to the equation:

$$|H_c(j\omega)|^2 = \frac{1}{1 + (\frac{\omega}{\omega_c})^{2N}} \tag{1}$$

where $|H_c(j\omega)|^2$ is the squared magnitude response, ω is the system frequency, ω_c is the cutoff frequency and N is the order of the filter. At low frequencies ($\omega_c >> \omega$) the magnitude response is nearly one while at high frequencies ($\omega >> \omega_c$) the magnitude response approaches zero. The magnitude of the system response monotonically decreases between the passband and stopband with more rapid rolloff rates associated with higher order filters. The frequency response shown in Figure 3 was chosen to provide minimum attenuation for frequencies up to 2000 Hertz.
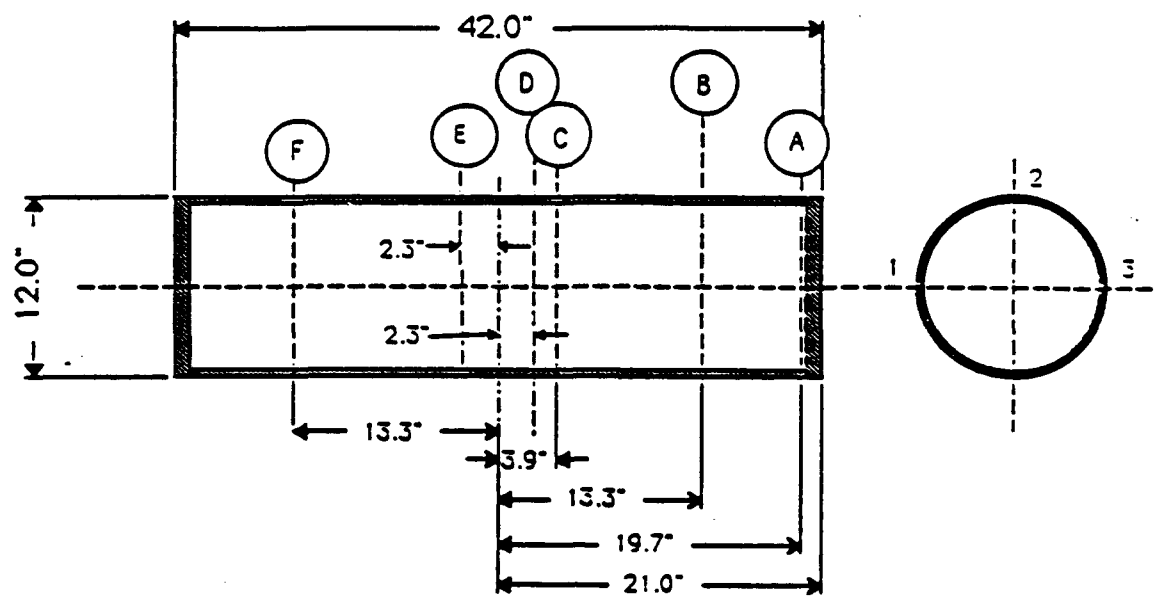
4

A1A: Axial strain at gage location A and radial position 1.
A1C: Hoop strain at gage location A and radial position 1.
A2A: Axial strain at gage location A and radial position 2.
A2C: Hoop strain at gage location A and radial position 2.
B2A: Axial strain at gage location B and radial position 2.
B2C: Hoop strain at gage location B and radial position 2.
B3A: Axial strain at gage location B and radial position 3.
B3C: Hoop strain at gage location B and radial position 3.
C1A: Axial strain at gage location C and radial position 1.
C1C: Hoop strain at gage location C and radial position 1.
C2A: Axial strain at gage location C and radial position 2.
C2C: Hoop strain at gage location C and radial position 2.
D3A: Axial strain at gage location D and radial position 3.
D3C: Hoop strain at gage location D and radial position 3.
E2A: Axial strain at gage location E and radial position 2.
E2C: Hoop strain at gage location E and radial position 2.
F1A: Axial strain at gage location F and radial position 1.
F1C: Hoop strain at gage location F and radial position 1.
F3A: Axial strain at gage location F and radial position 3.
F3C: Hoop strain at gage location F and radial position 3.

Figure 1. Instrumentation Locations for End-On Cylinder
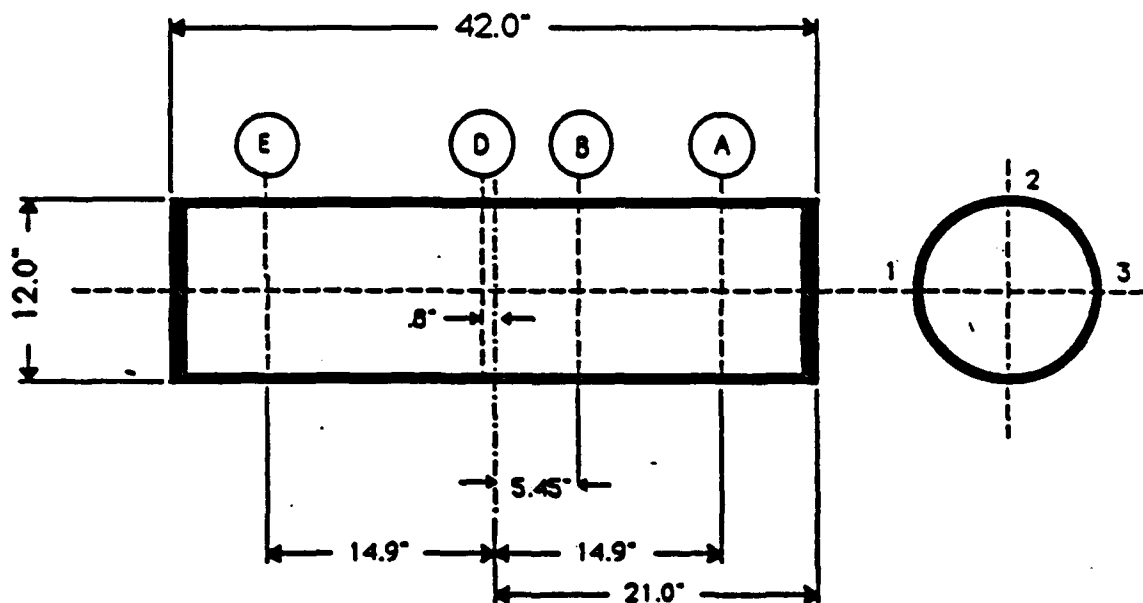
5

A1A: Axial strain at gage location A and radial position 1.
A1C: Hoop strain at gage location A and radial position 1.
A2A: Axial strain at gage location A and radial position 2.
A2C: Hoop strain at gage location A and radial position 2.
B1A: Axial strain at gage location B and radial position 1.
B1C: Hoop strain at gage location B and radial position 1.
B2A: Axial strain at gage location B and radial position 2.
B2C: Hoop strain at gage location B and radial position 2.
B3A: Axial strain at gage location B and radial position 3.
B3C: Hoop strain at gage location B and radial position 3.
D2A: Axial strain at gage location D and radial position 2.
D2C: Hoop strain at gage location D and radial position 2.
D3A: Axial strain at gage location D and radial position 3.
D3C: Hoop strain at gage location D and radial position 3.
E1A: Axial strain at gage location E and radial position 1.
E1C: Hoop strain at gage location E and radial position 1.
E2A: Axial strain at gage location E and radial position 2.
E2C: Hoop strain at gage location E and radial position 2.

Figure 2. Instrumentation Locations for Side-On Cylinder

6

A. TEST OBJECTIVES AND PHYSICAL ARRANGEMENT

The objective of this shock test was to locate the aluminum cylinders closer to the explosive charge than in the August 1991 test so as to create visible plastic deformation of the cylinders. The magnitude of these deformations, as well as the cylinder response as measured by the strain gages, were to be compared with numerical predictions to assist in understanding the physics of this dynamic fluid-structure interaction.
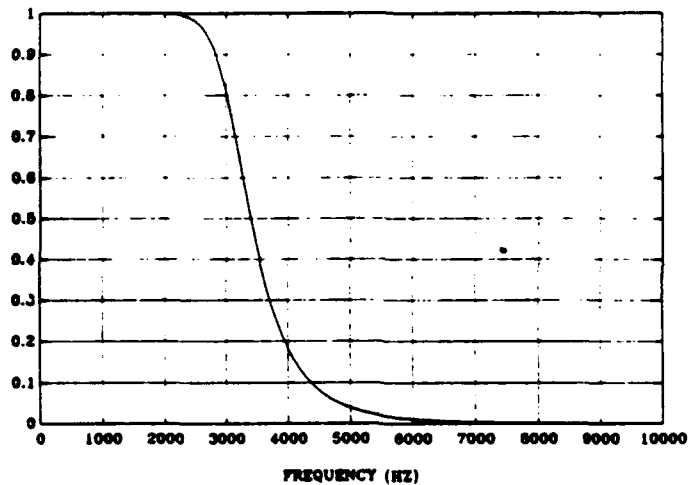
Figure 3. Frequency Response of Butterworth Digital Filter

The physical arrangement for the shock test is shown in Figure 4. Two free-field pressure transducers and the two instrumented cylinders were located at a range of 15 feet from the explosive charge. Standoff range was maintained with steel wires between the cylinders and charge which were attached to shoreline connection points. A third free-field pressure transducer was located three feet from the leading edge of the end-on

7

cylinder to provide redundancy in pressure measurement. Pressure transducers P1 and P2 were located on the surface of the cylinders closest to the charge to measure shock wave arrival time. The cylinders, explosive charge, and pressure transducers were located 10 feet below the surface, as shown in Figure 5. Weights were suspended from cylinder endplate padeyes to provide negative buoyancy. Steel wire attached to floats ensured the desired depth and attack geometry were maintained during the test.

B.   EXPERIMENTAL PROBLEMS

A high peak shock wave pressure and recording equipment set-up errors resulted in a considerable loss of experimental data. Two of three free-field pressure transducers and three strain gages failed to provide any output data. Eleven of the remaining 35 strain gages displayed evidence of amplifier saturation due to gage failure or actual strain conditions in excess of recording device response.

Two of the three free-field pressure transducers installed in this experiment provided no pressure-time history data. Transducer P4 recorded the pressure profile shown in Figure 6. Peak shock wave pressure was noted to be 4163 psi. An approximately exponential decay in shock wave pressure occurred up to 1.18 milliseconds. The second peak and subsequent disturbance occurred too early to be a result of the fluid-structure interaction and is most likely due to a loose transducer connection. To correct for this instrument anomaly, a linear interpolation of the pressure-time history values was performed from 1.18 milliseconds until surface cutoff occurred
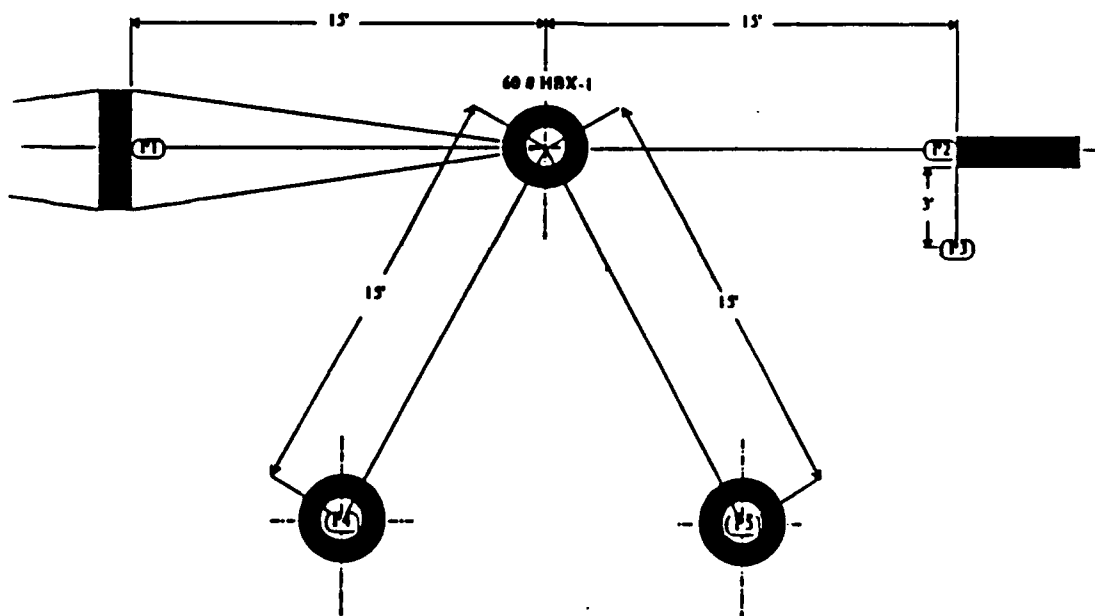
Figure 4. UNDEX Test Geometry (Plan View)

SURFACE

10 FT.

15 FT.   15 FT.

SIDE-ON   CHARGE   END-ON
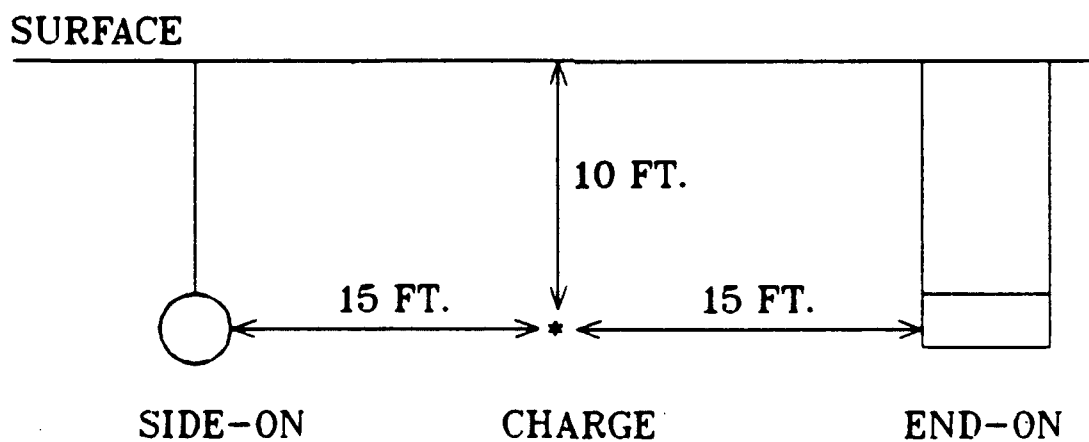
Figure 5. UNDEX Test Geometry (Elevation View)

9

at 2.08 milliseconds. This corrected pressure-time history was used to develop subsequent numerical results.

Sixteen of the twenty strain gages installed on the cylinder subjected to axial (end-on) attack provided usable strain information for ten milliseconds of response time. The two gages installed to measure hoop strain at locations B2 and C2 and one gage installed to measure axial strain at location B3 failed shortly after water immersion. These gages provided no strain information. The axial strain gage output at location C1 showed evidence of amplifier saturation four milliseconds after shock wave arrival. The hoop strain gage at location D3 failed at approximately ten milliseconds.

Nine of eighteen strain gages installed on the cylinder subjected to side-on attack provided usable strain information for ten milliseconds of response time. Local fractures in the cylinder caused three broken wires, which resulted in loss of all strain data from location A1 and hoop strain data from location E2. The four gages installed to measure hoop strain at locations A2, B2, and D3 and axial strain at location E2 failed within one millisecond after shock wave arrival. Strain gage output for axial strain at location B2 and hoop strain at location D3 saturated the output amplifiers within the first three milliseconds and provided unreliable data thereafter.

Although fractures in both cylinders accounted for some unexpectedly high strain readings, most of the problems with amplifier saturation occurred well below the anticipated maximum strain value of 50,000 microstrain. In fact, ten of eleven strain gage output readings which exhibited amplifier saturation occurred at 30,000 microstrain or

below which indicates recording equipment set-up errors. This data will not be presented

in this section.
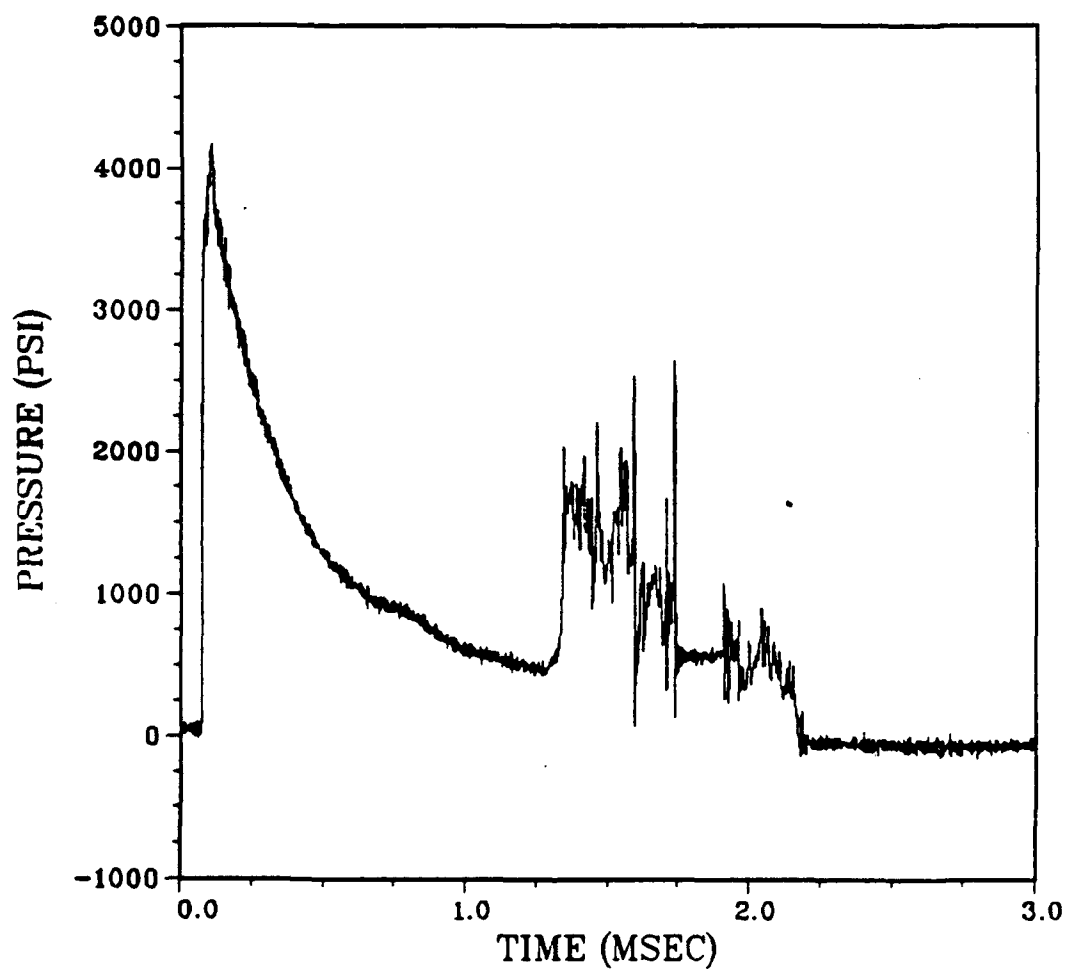
Figure 6. Free-Field Pressure History

C. NUMERICAL MODEL

1. Theory and Code Description of USA/DYNA3D

The computation of cylinder response to an underwater shock wave was accomplished by two different domain discretization techniques. The structural response of the cylinder was computed using the finite element method. This method, however, is not efficient for modeling the surrounding water. The large volume of water between the explosive charge and cylinder would require an excessive number of elements to model. To solve this problem, the surrounding water was modeled through the use of the boundary element method.

The use of the boundary element method avoids the discretization of the water volume by determination of the equivalent forces and masses imparted to the cylinder by the water. These forces and masses are applied at the nodes of a two dimensional mesh. This mesh is then superimposed over the cylinder surface. As a result, significantly fewer elements are required to model the fluid-structure interaction which results in better computational efficiency.

The finite element code chosen for this analysis was the VEC/DYNA3D (Nonlinear Dynamic Analysis of Structures in Three Dimensions) code [Ref. 2]. This explicit finite element code has been widely used in analysis of the dynamic response of structures since its introduction in 1976. A wide array of material models and equations of state are included in this code to provide a high degree of modeling flexibility.

12

The VEC/DYNA3D code is operational on workstations and mainframe computer systems including the Los Alamos CRAY computer. This wide code availability accommodates problems with varying degrees of complexity. Problems which required over 13,000 elements have been run on IBM RISC 6000 workstations at the Naval Postgraduate School. Code availability is further enhanced in that VEC/DYNA3D is a public domain program.

Three dimensional mesh generation for VEC/DYNA3D is provided by the LS-INGRID pre-processor [Ref. 3]. The output display of contours, fringe plots and time histories is provided by the LS-TAURUS post-processor [Ref. 4]. Both of these processors provide interactive graphics capability for the user.

The boundary element code used in this analysis was the Underwater Shock Analysis (USA) code [Ref. 5]. The USA code calculates the transient response of a submerged structure to an underwater shock wave through use of the Doubly Asymptotic Approximation (DAA) [Ref. 6]. This approximation is used to determine the fluid pressure due to the scattered acoustic wave on the surface of the structure.

The capability to calculate shock-induced dynamic responses of submerged structures was accomplished by coupling the USA (Underwater Shock Analysis) code with the VEC/DYNA3D code. This code combination was made in 1991 at the request of the Naval Postgraduate School. Verification of the satisfactory performance of the combined USA/DYNA3D codes was recently conducted for spherical and infinite

cylinder models by Fox [Ref. 7]. The results of this thesis represent the second underwater explosion test analyzed with the combined USA/DYNA3D codes.

The differential equation for dynamic response of a structure can be expressed as:

$$[M_s]\{\ddot{x}\} + [C_s]\{\dot{x}\} + [K_s]\{x\} = \{f\} \qquad (2)$$

where $[M_s]$, $[C_s]$, and $[K_s]$ are the structural mass, damping, and stiffness matrices, respectively. The vectors of nodal displacement, velocity and acceleration are denoted by $\{x\}$, $\{\dot{x}\}$ and $\{\ddot{x}\}$. The external force vector is denoted by $\{f\}$. This external force is related to the incident and scattered acoustic wave pressure by the relation:

$$\{f\} = -[G][A_f]\{P_i + P_s\} + \{f_D\} \qquad (3)$$

where P_i and P_s are incident and scattered pressure vectors, respectively, $[G]$ is a force transformation matrix, $[A_f]$ is a diagonal area matrix associated with the fluid mesh elements and $\{f_D\}$ is the dry structure applied force vector.

The only unknown in the preceding equation is the scattered pressure which can be determined from a first order differential equation of the form

$$[M_f]\{\dot{P}_s\} + \rho c [A_f]\{P_s\} = \rho c [M_f]\{\dot{u}_s\} \qquad (4)$$

where $[M_f]$, ρ, c, and $\{\dot{u}_s\}$ are the symmetric fluid mass matrix, fluid density, sound velocity, and particle velocity normal to the wet surface, respectively. The solution to this differential equation asymptotically approaches a high frequency and low frequency limit.

Acoustic waves will be scattered off a structure with little pressure loss since the structure acts as a nearly rigid boundary. For high frequency acoustic waves, $|P_s| >> |\dot{P}_s|$. The first order differential equation approaches the plane wave approximation of

$$\{P_s\} = \rho c \{u_s\}$$ (5)

in the limit following integration with respect to time.

For low frequency acoustic waves, $|P_s| << |\dot{P}_s|$. In the low frequency limit, the scattered wave pressure differential equation reduces to

$$[A_f]\{P_s\} = [M_f]\{\ddot{u}_s\}$$ (6)

which is known as the virtual mass approximation. A smooth transition is effected between the asymptotic values by DAA relations.

An extension of the above relations was developed to account for surface curvature effects. This extension, known as DAA2, requires a second order differential equation to describe the scattered wave pressure. The theory for DAA2 is contained in [Ref. 8].

2.   Model Description

One finite element model was used to approximate the dimensions of the instrumented cylinders. An elastic-plastic material model available in VEC/DYNA3D was chosen for the numerical analysis. Strain rate effects were neglected in this model because of the low strain rate sensitivity of aluminum. Values for Young's modulus and yield stress of 10,800 ksi and 40 ksi, respectively, were used for this analysis. The half-

15

cylinder model was constructed using 544 Belytschko-Lin-Tsay shell [Ref. 9] elements with three-point quadrature through the shell thickness. An additional 32 elements were used to discretize the internal ring stiffener. This model is shown in Figure 7.
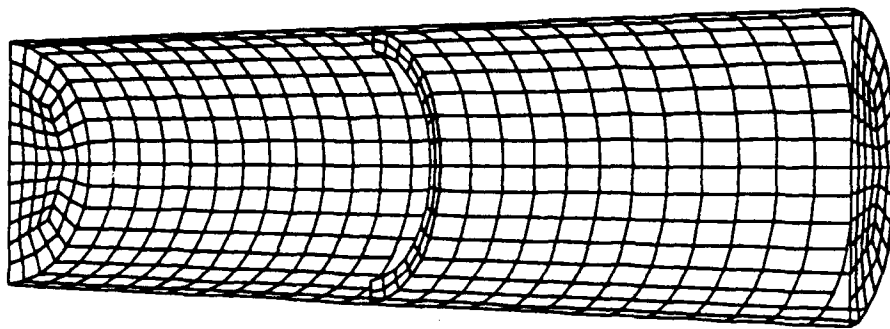

Figure 7. Ring-Stiffened Half Cylinder Model

D. COMPARATIVE RESULTS AND ANALYSIS

A comparison of experimental and numerical strain values was conducted to determine the usefulness of numerical techniques to aid in understanding the transient, nonlinear response of a cylinder subjected to an underwater explosion. The complex behavior of shells subjected to explosive loads makes test design difficult. The response of both cylinders to the explosive loading in this test was more severe than expected and resulted in cylinder failure in both cases. Not surprisingly, poor agreement was seen in the vicinity of cylinder cracks. However, the presence of the ring stiffeners limited the scope of the damage in both cylinders and resulted in good qualitative comparisons at gage locations remote from the failure zones.

1. End-On Attack Geometry

The cylinder subjected to the end-on shock wave suffered severe plastic deformation and collapse due to weld failure at the cylinder end nearest to the charge. The weld failure occurred near the longitudinal axis which contained strain gages B3, D3, and F3. As a result, strain gage readings from these three instruments were most severely affected by the material failure. A six-inch section of the aluminum cylinder located between gage locations 2 and 3 was physically separated from the near endplate due to the force of the shock wave. A large crack extended the length of the cylinder beginning at the location of the weld failure. The ring stiffener was fractured with evidence of heavy plastic deformation prior to failure. Two additional cracks in the circumferential direction were also noted near the ring stiffener. In addition, a six-inch length of cylinder displayed local buckling near the locations of gages A2 and B2.

17

Despite the global nature of the failure in this cylinder, instrumented locations remote to the failure area behaved nearly as expected by the numerical analysis. The presence of the ring stiffener undoubtedly confined the damage caused by the failure and aided in preserving the geometry of the cylinder. A picture of the damaged cylinder is shown in Figure 8. End-on explosion strain-time history results are presented in Figures 9 through 24.

As discussed by Boticario [Ref. 10], the symmetric axial loading of this cylinder was expected to produce axially symmetric deformations. A comparison of axial and hoop strains at locations A1 (Figures 9 and $\therefore$ and A2 (Figures 11 and 12) show poor agreement with this expected behavior. The gages at locations F1 (Figures 21 and 22) and location F3 (Figures 23 and 24) also fail to support the expected behavior. Comparisons of hoop strain at these locations showed the greatest errors.

The cylinder failure near strain gage locations B3, D3 and F3 had a significant effect on the experimental results. Axial strain for gages D3 (Figure 17) and F3 (Figure 23) were smaller in magnitude than expected from the numerical model which did not incorporate failure criteria. The stress relief which occurred as a result of the nearby failure would account for these low strain values. Hoop strain at location B3 (Figure 14) was significantly greater than the predicted value due to the collapse of the cylinder walls in the immediate area. In contrast, the hoop strain at location D3 (Figure 18) was lower in magnitude than the predicted value due to nearby failure of the ring stiffener. Axial and hoop strain values at gage location F3 (Figures 23 and 24) were also smaller than expected due to the stress relief afforded by the nearby crack.

Figure 8. Damaged Cylinder Following End-On Attack .
(Lower Endplate Closest to Charge)

and hoop strain values at gage location F3 (Figures 23 and 24) were also smaller than expected due to the stress relief afforded by the nearby crack.
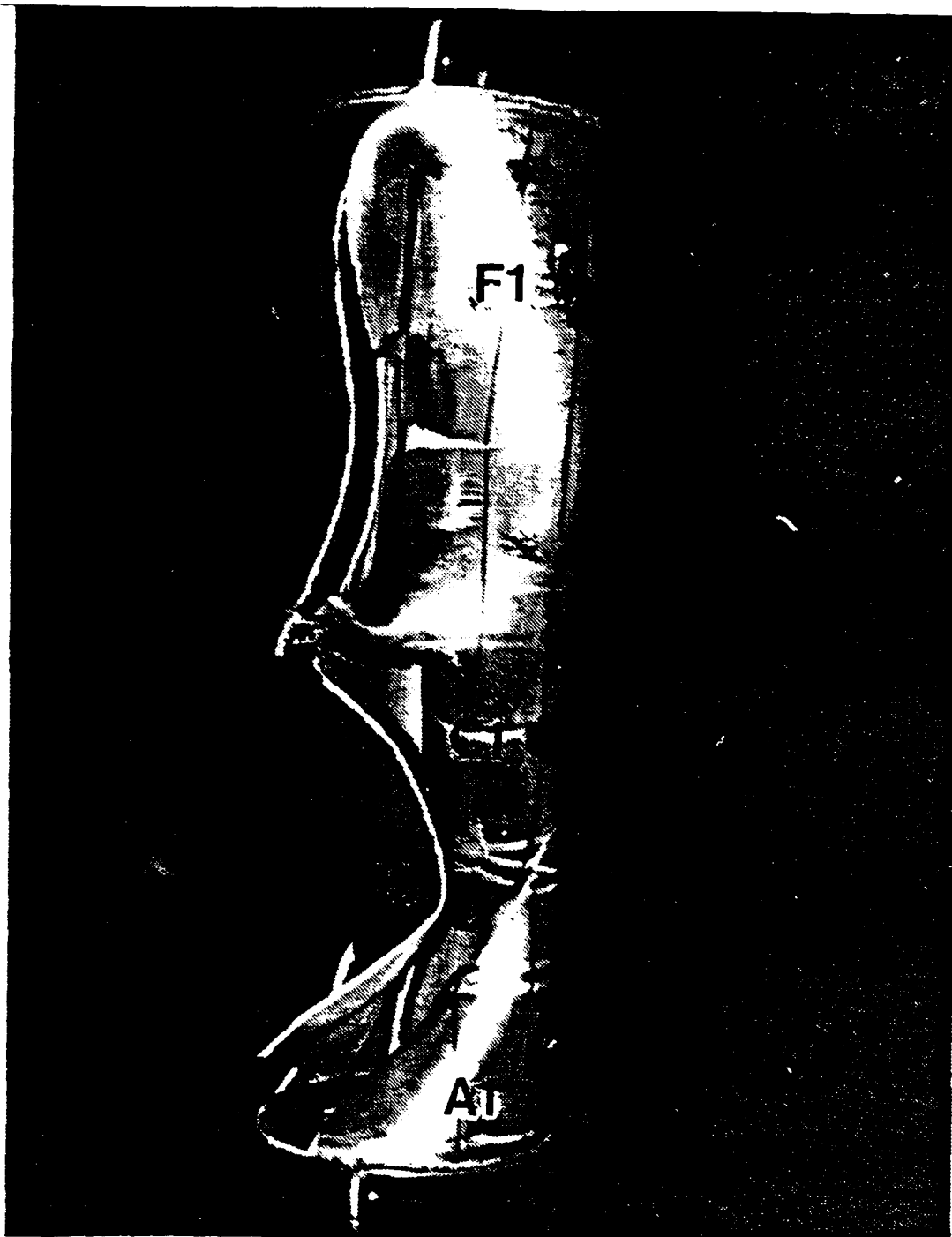
Strain comparisons at other locations on the cylinder (Figures 13, 15, 16, 19 and 20) were in fairly good agreement. The largest deviations occurred at gage locations near the ends of the cylinder where strain magnitudes were expected to be maximum. The local buckling observed at location A2 was more severe than the expected value which resulted in a poor quantitative comparison of hoop strain (Figure 12). The axial and hoop strain values at location F1 (Figures 21 and 22) were smaller in magnitude than expected but still showed good qualitative agreement.

The weld failure and subsequent crack propagation seems to have occurred approximately two milliseconds after shock wave arrival. The best indication of the time of failure can be seen at location B3 (Figure 14). Normally, the maximum compressive hoop strain occurs within the first millisecond after shock wave arrival. In this case, the maximum compressive strain occurred well after two milliseconds. The good correlation between actual and predicted strain values up to two milliseconds indicate that cylinder integrity was probably maintained until this time.

Figure 9. End-On Explosion Axial Strain at Gage Location A1

Figure 10. End-On Explosion Hoop Strain at Gage Location A1

21

Figure 11. End-On Explosion Axial Strain at Gage Location A2

Figure 12. End-On Explosion Hoop Strain at Gage Location A2

Figure 13. End-On Explosion Axial Strain at Gage Location B2

Figure 14. End-On Explosion Hoop Strain at Gage Location B3

Figure 15. End-On Explosion Hoop Strain at Gage Location C1

Figure 16. End-On Explosion Axial Strain at Gage Location C2

24

Figure 17. End-On Explosion Axial Strain at Gage Location D3

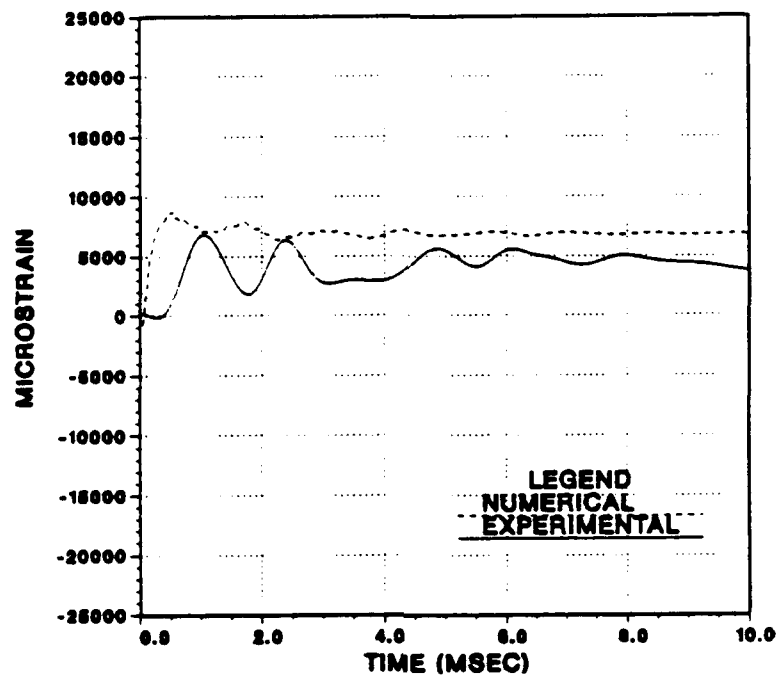**Figure 18.** End-On Explosion Hoop Strain at Gage Location D3

25

Figure 19. End-On Explosion Axial Strain at Gage Location E2

Figure 20. End-On Explosion Hoop Strain at Gage Location E2

Figure 21. End-On Explosion Axial Strain at Gage Location F1
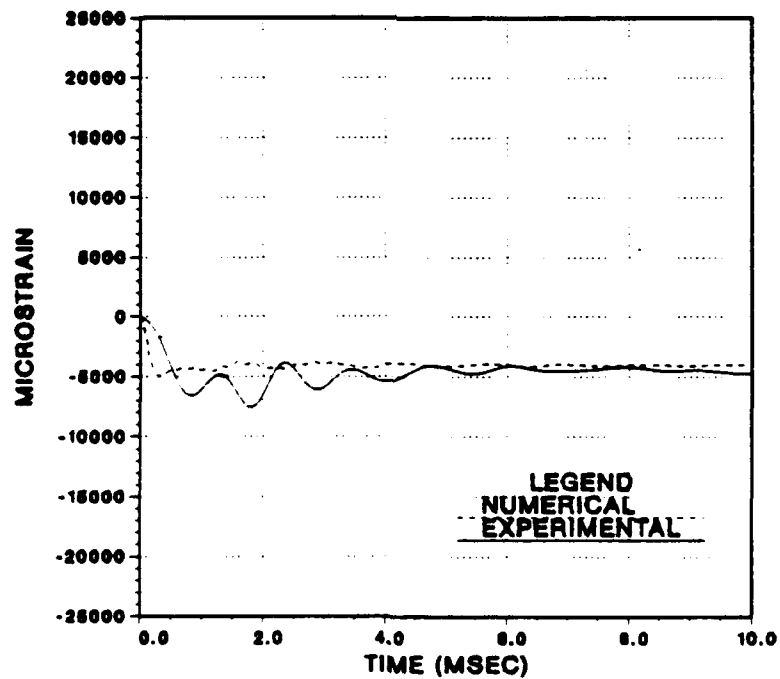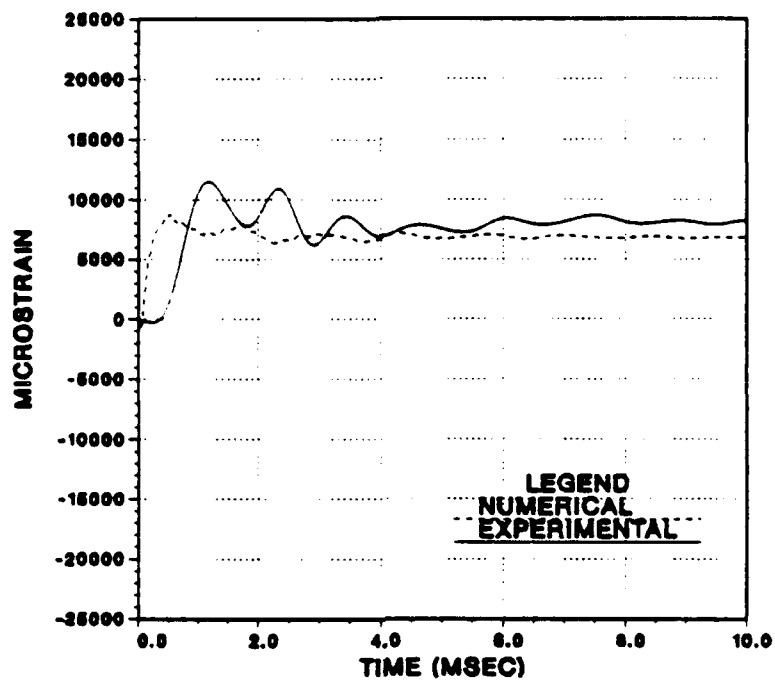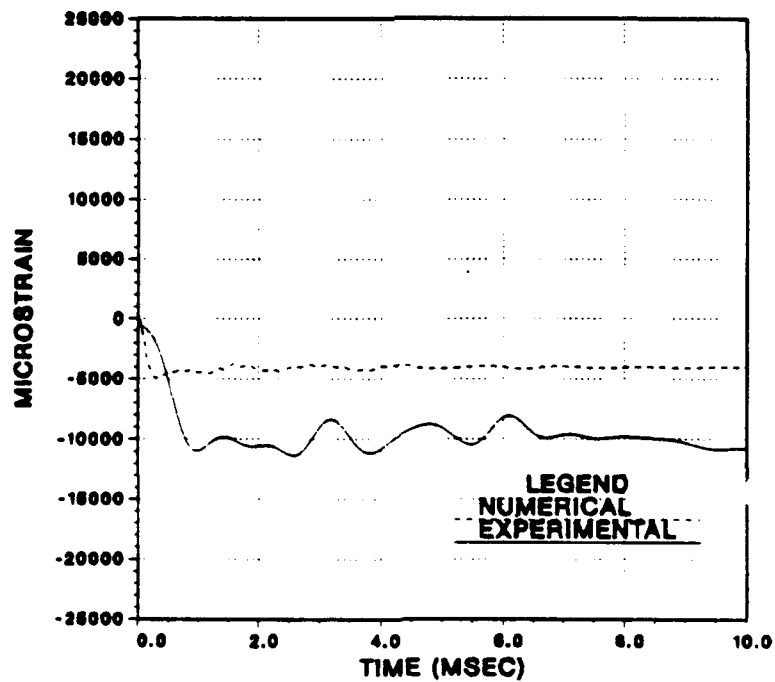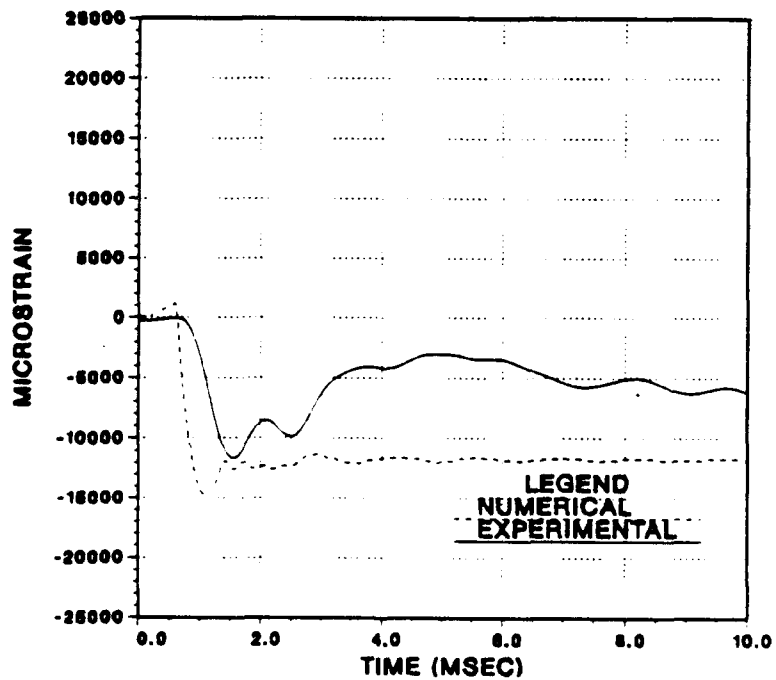

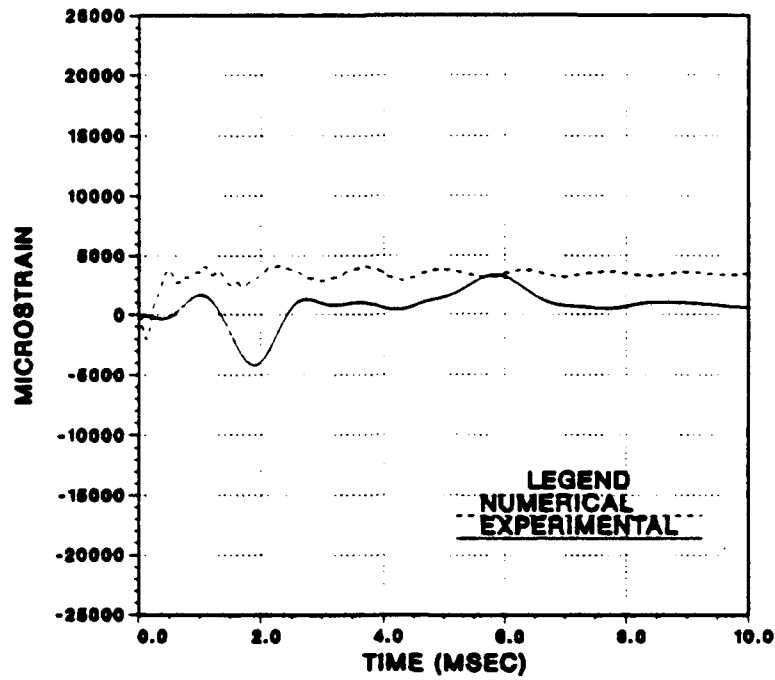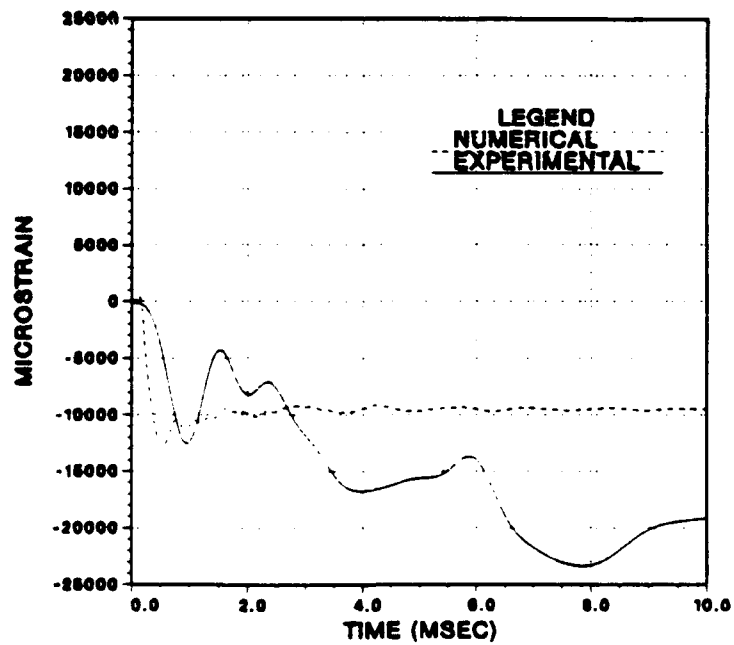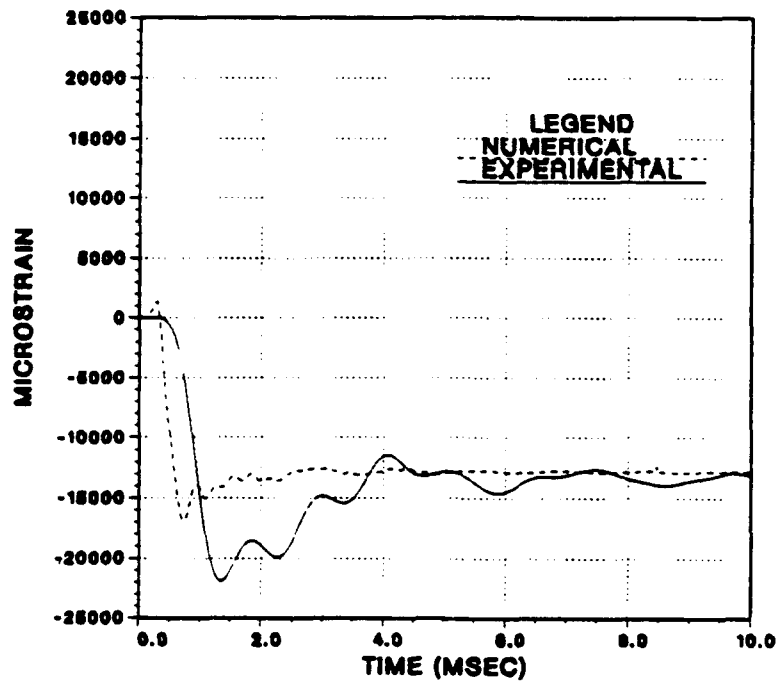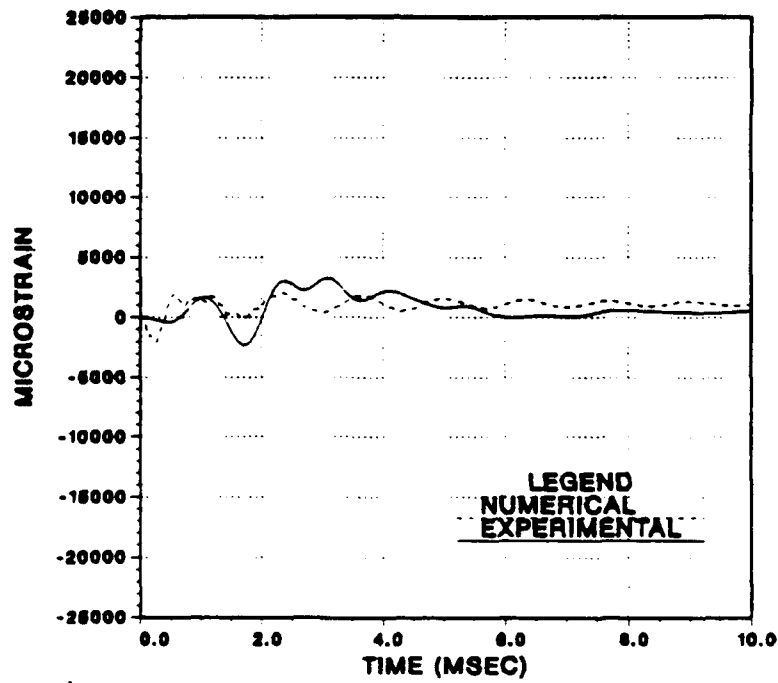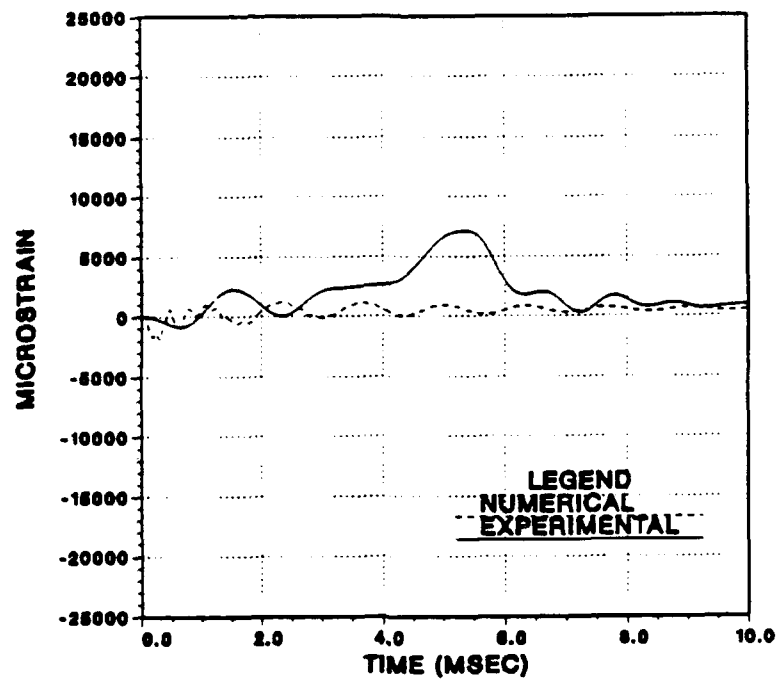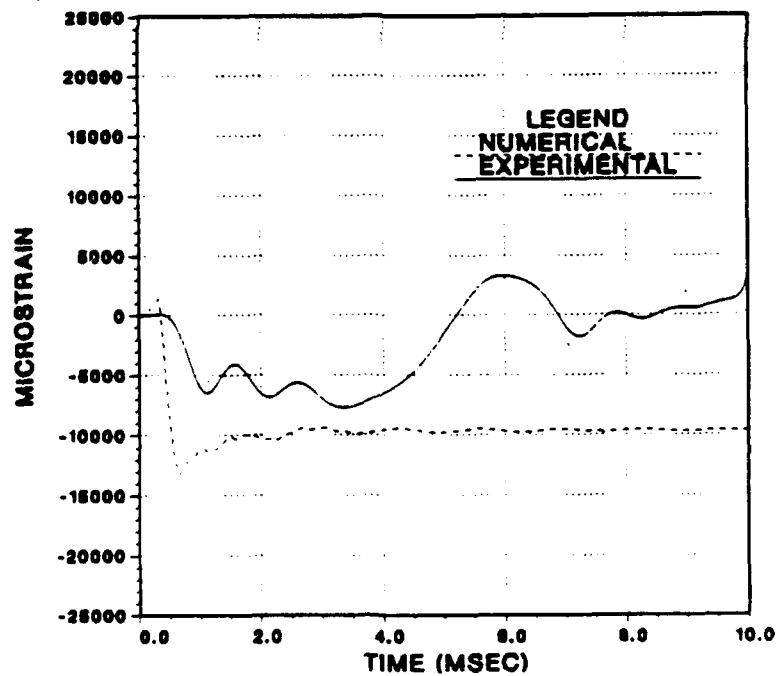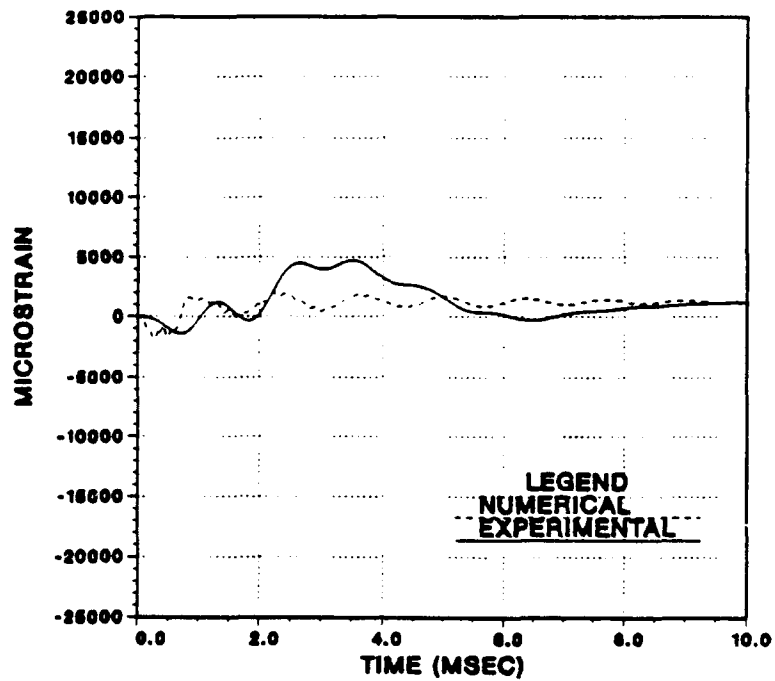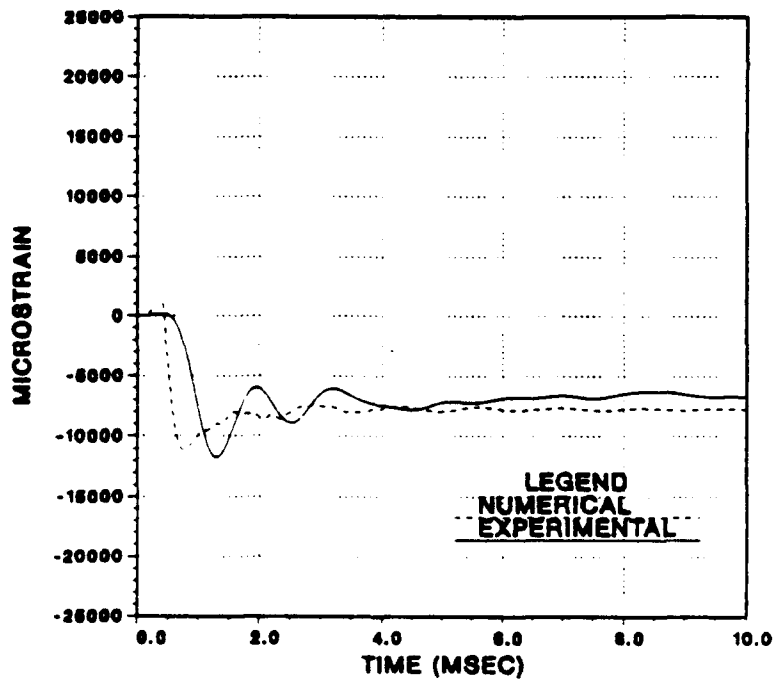**Figure 22.** End-On Explosion Hoop Strain at Gage Location F1

27

Figure 23. End-On Explosion Axial Strain at Gage Location F3

Figure 24. End-On Explosion Hoop Strain at Gage Location F3

28

2. Side-On Attack Geometry

The cylinder subjected to the side-on attack also displayed cracks and local buckling in several areas. The top of the cylinder near gage location axis 2 displayed fairly symmetric cracks on both sides of the ring stiffener. The cylinder was ruptured between gage locations A2 and B2. Local buckling was noted in several places on the bottom of the cylinder. A picture of the damaged cylinder is shown in Figure 25. Side-on explosion strain-time history results are shown in Figures 26 through 35.

The stress relief and resultant low values of plastic strain near the cylinder cracks (location 2) was observed as in the end-on attack case. Axial strains at locations A2 (Figure 27) and D2 (Figure 32) show very little plastic deformation. Other strain information at this location was lost due to gage failure.

Strain information at the front (location 1) and back (location 3) of the cylinder was in good qualitative agreement with the numerical predictions. Comparisons of strain results at locations B1 (Figures 28 and 29), B3 (Figures 30 and 31), and D3 (Figure 33) illustrate this observation. As noted in the end-on attack case the geometry of the cylinder was effectively maintained by the ring stiffener. Thus, the final strain values far from the failure zone were not significantly affected by the fractures. However, the transient response of the cylinder was clearly affected shortly after the occurrence of the failures.

The failures in the cylinder probably began about 1.5 milliseconds after shock wave arrival. As previously mentioned, the strain gage output from location A1 was lost when gage wires were severed by a nearby cylinder crack. The axial strain plot at

29

location A1 (Figure 26) showed large compressive strain at about 1.5 milliseconds followed by a rapid rise to tensile strain. The oscillations noted at about 3.0 milliseconds are a consequence of the Butterworth filtering technique and are not indicative of actual strain at this location. Unfiltered data showed that this excursion into tensile strain was a result of gage failure. Therefore, the large axial compressive strain in the cylinder at 1.5 milliseconds was quickly followed by the material failures.

The tensile hoop strain observed at gage location E1 (Figure 35) was not well-predicted by the numerical model. The stiffness of the endplate and high inertial force which it imparts to the cylinder walls should produce a compressive hoop strain at this location. Sensitivity analyses with attack geometry variations and mesh density effects were investigated in an attempt to explain this behavior. The lack of reliable strain data at symmetric locations A1 and E3 hampered further analysis. Axial strain results at location E1 (Figure 34) were also quite different. Most likely, the behavior at location E1 was a result of the failures near locations D2 and E2 at top of the cylinder. This effect will be discussed in more detail in section IV.
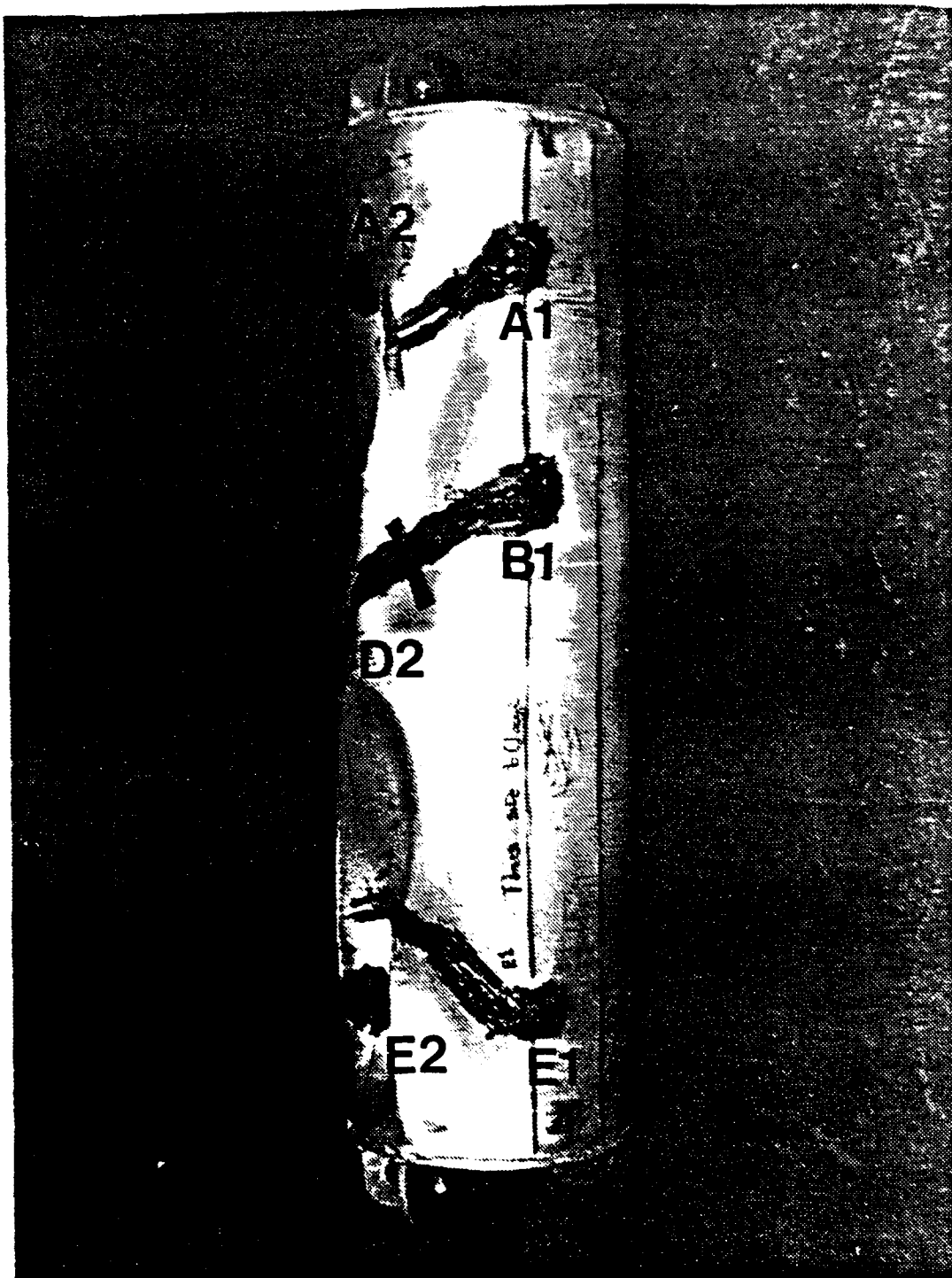
Figure 25. Damaged Cylinder Subjected to Side-On Attack
(Charge Location to Right of Cylinder)

31
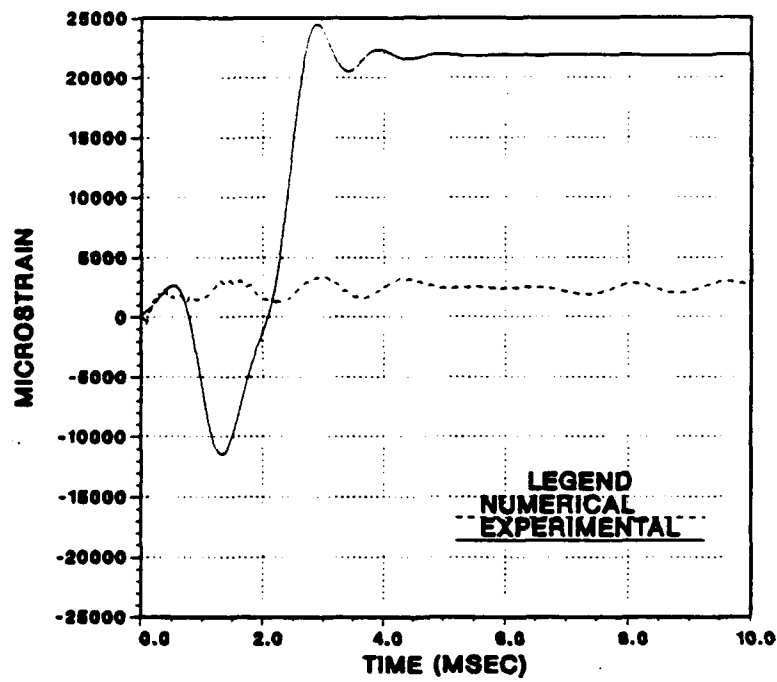
Figure 26. Side-On Explosion Axial Strain at Gage Location A1
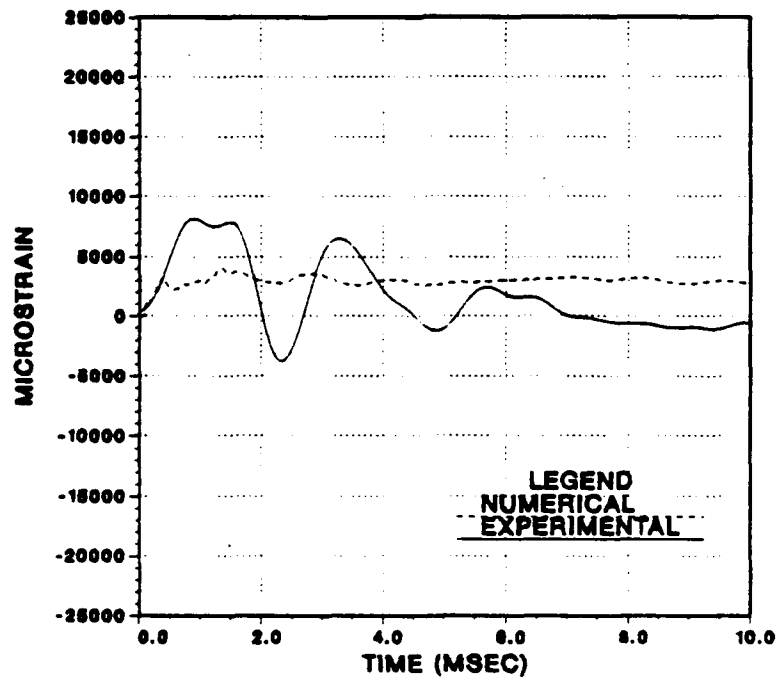
Figure 27. Side-On Explosion Axial Strain at Gage Location A2
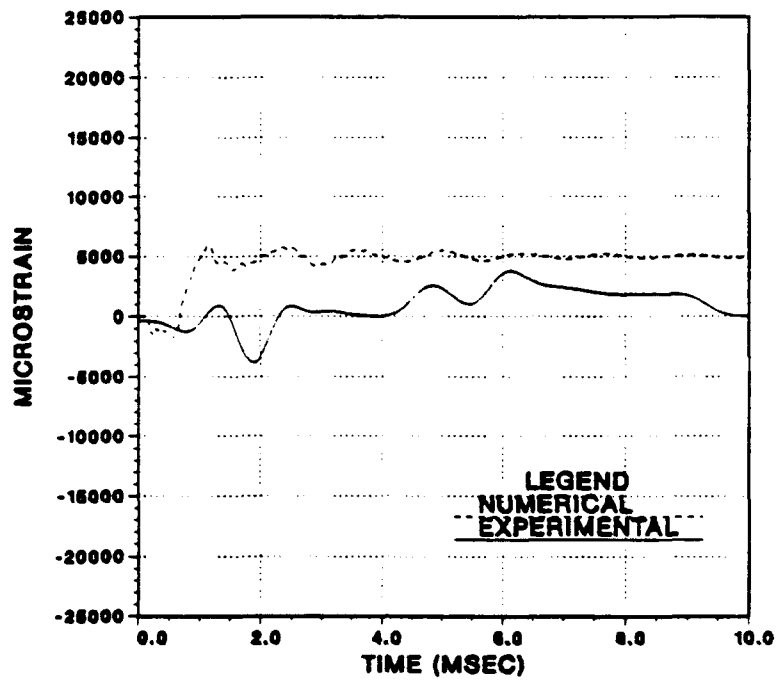
32
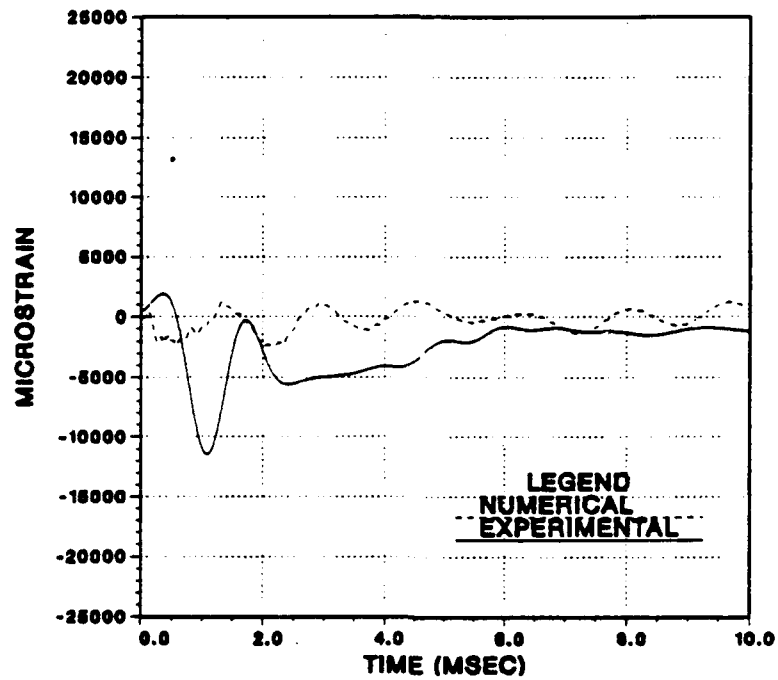
Figure 28. Side-On Explosion Axial Strain at Gage Location B1
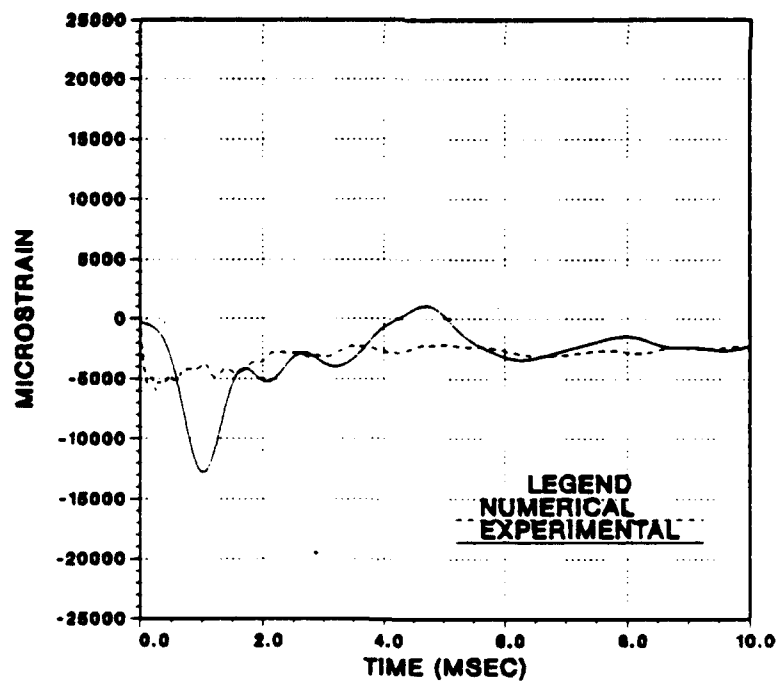
Figure 29. Side-On Explosion Hoop Strain at Gage Location B1

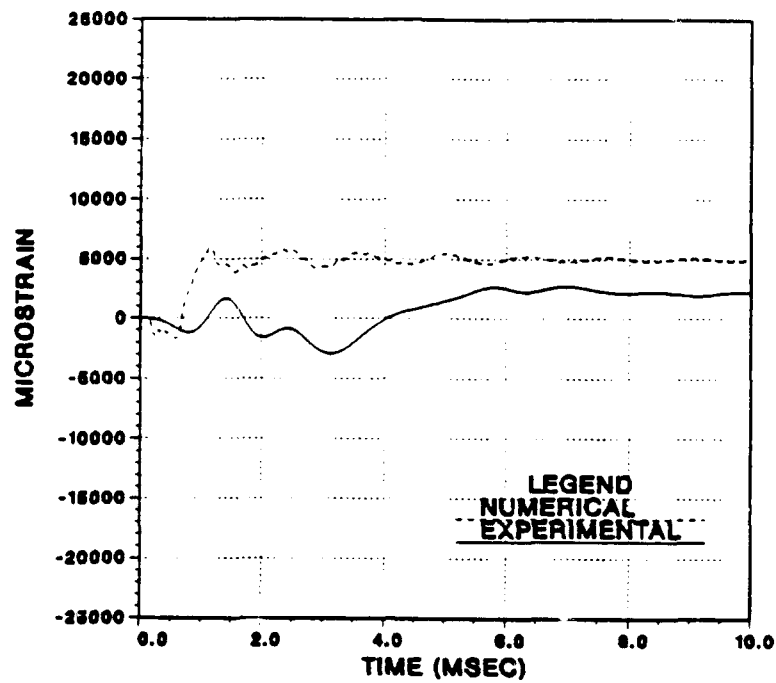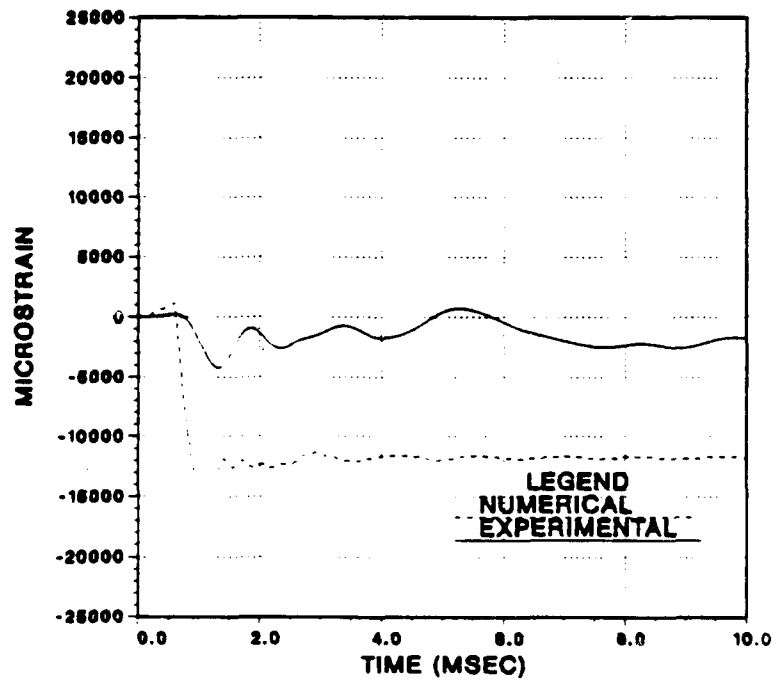33
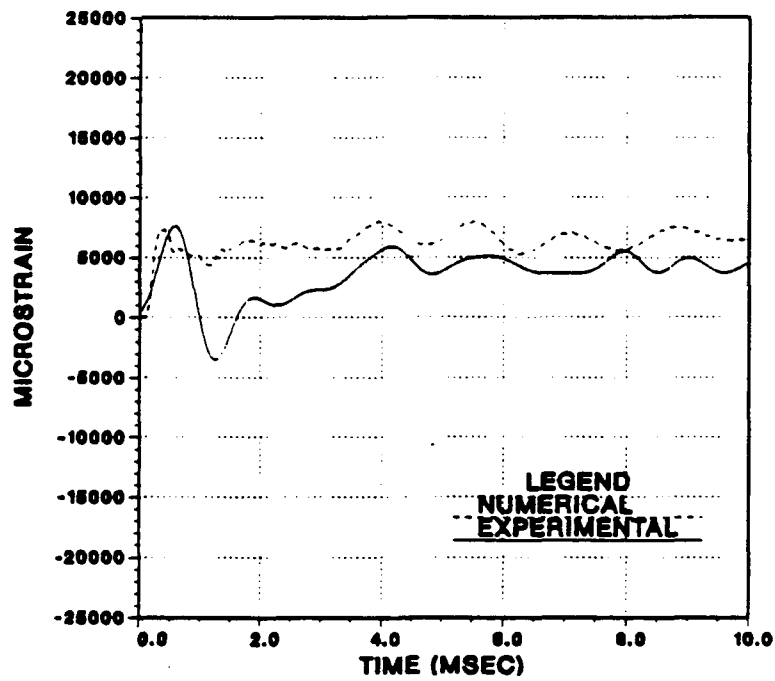
Figure 30. Side-On Explosion Axial Strain at Gage Location B3
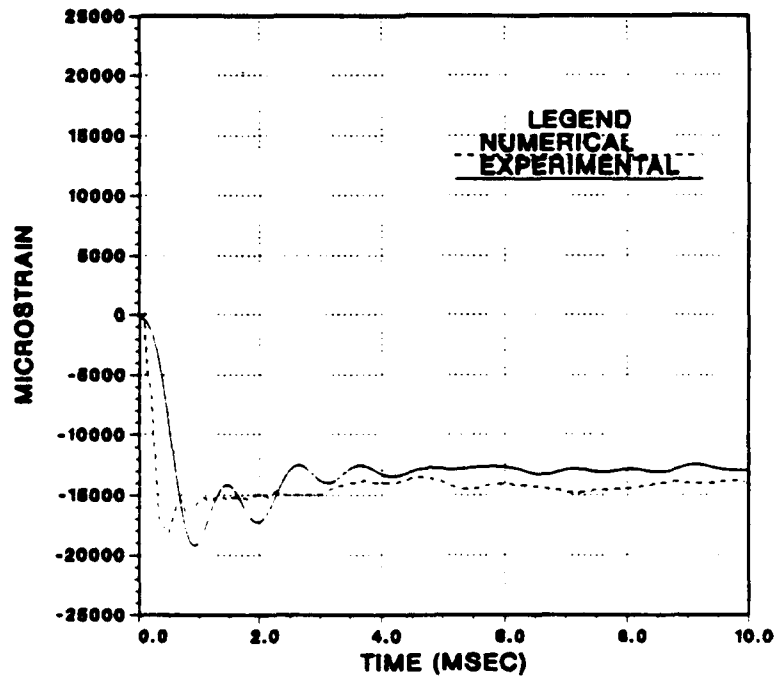
Figure 31. Side-On Explosion Hoop Strain at Gage Location B3

34
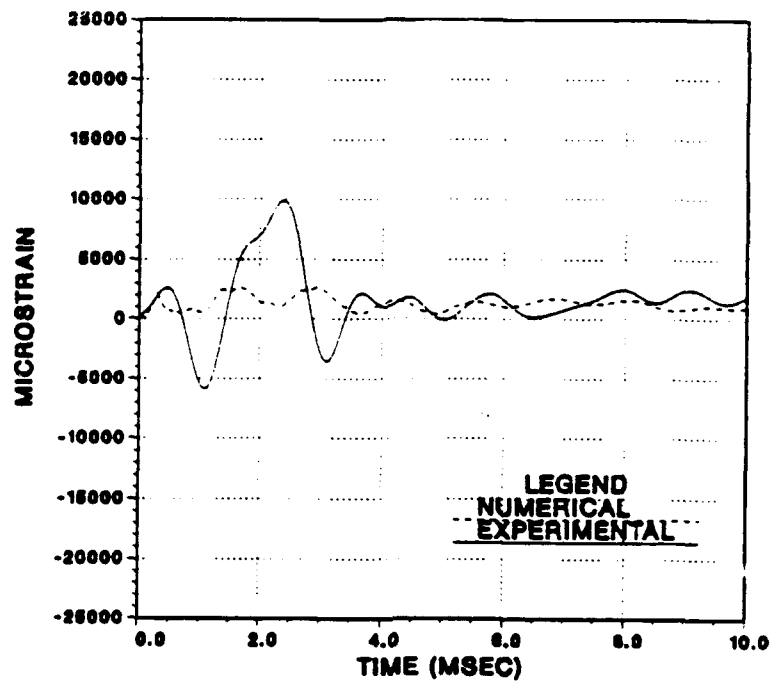
Figure 32. Side-On Explosion Axial Strain at Gage Location D2
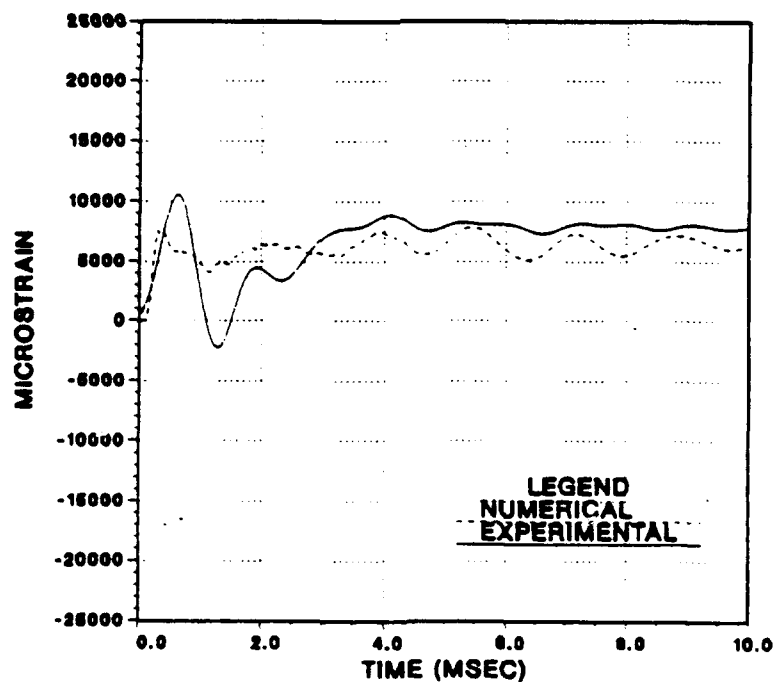
Figure 33. Side-On Explosion Axial Strain at Gage Location D3
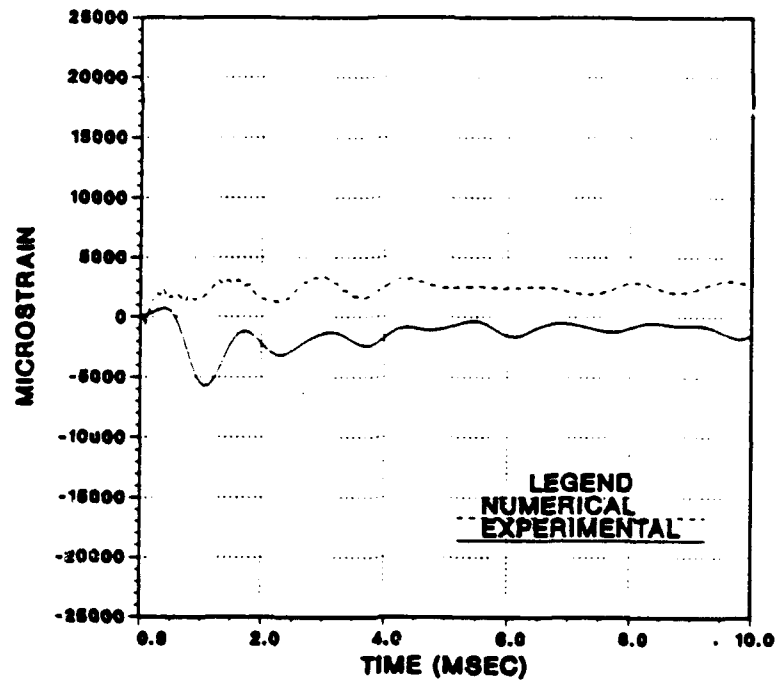
Figure 34. Side-On Explosion Axial Strain at Gage Location E1
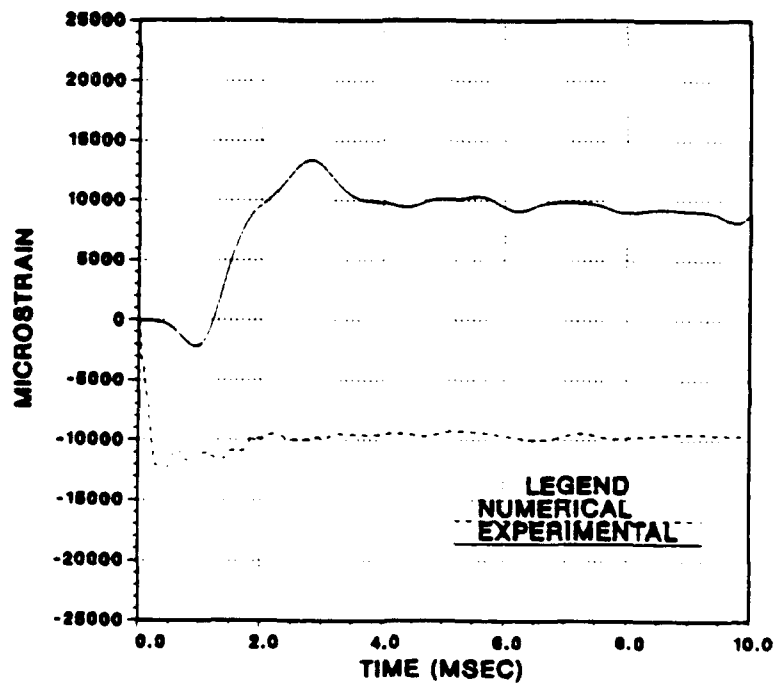
Figure 35. Side-On Explosion Hoop Strain at Gage Location E1

36

III. SENSITIVITY ANALYSIS OF CYLINDER RESPONSE

Three parameters in the acquisition of experimental and numerical strain values were varied to determine response sensitivity. A shell element numerical model was compared with two other models using different finite element formulations. Strain values for the end-on and side-on attack geometries were computed with the assumption of cylinder misalignment due to rotations of up to 10 degrees. Finally, the numerical model mesh density was varied to determine solution sensitivity to finite element size.

A. VARIATIONS IN FINITE ELEMENT MODEL CONSTRUCTION

The sensitivity of the numerical strain values to the type of finite elements used in model construction was evaluated using three different models. The first model, known as the shell model, used four node shell elements for cylinder and endplate construction. The second model, known as the combination model, used four node shell elements for the cylinder but eight node thick shell elements for the endplates. The third model, known as the thick shell model, employed eight node thick shell elements for both cylinder and endplate construction.

For computational efficiency, an unstiffened quarter model was used for this analysis. The 60 pound HBX-1 charge was simulated at 15 feet from the cylinder in an end-on attack orientation. Model depth was set at 10 feet as in the explosive test. The model contained 312 elements and had identical dimensions to the test specimen. The

same three point quadrature rule and integration time step was used in each model formulation. The model used in this analysis is shown in Figure 36.

The differences in model construction provided the theoretical basis for this analysis. The four node shell element is constructed with nodes placed along the mid-plane of the element. The connectivity requirements of nodes at the endplate and cylinder boundary causes these two mid-plane surfaces to be joined together. A more realistic representation of the actual test specimen was developed by the thick shell formulation where the inner endplate surface is connected to the cylinder at both upper and lower surface nodes. The combination model was a mixture of these two formulations to combine more realistic endplate modeling with the computational efficiency of shell elements.

The differences between these formulations led to strain prediction variations near the endplates known as end effects. These end effects occurred because the inertial effects and stiffness of the endplates caused the greatest strains to be located on the cylinder near the endplate and cylinder interface. As a result of element formulation, cylinder deformations were allowed to begin in different locations for these three models. Deformations in the shell model began at the mid-plane surface of the endplate whereas deformations began in the thick shell model at the inner surface of the cylinder endplate. The one-half inch difference in these positions resulted in significant variations in strain value prediction near the endplates.

The most significant variations in predicted strain values occurred in the hoop direction near the endplates. In most cases, major variations between the element models

occurred within 8.5 inches of the endplates. At locations closer to the center of the cylinder, end effects had a less significant effect on strain values. Finite element model comparisons are shown in Figures 37 through 46.

As discussed by Fox [Ref. 7], effects of the number of quadrature rule integration points and integration time step size is also a factor in the disparity of results in high strain areas. The use of a greater number of through-the-thickness integration points or a smaller time step was seen to cause shell and thick shell results to converge towards an intermediate value. The cost of obtaining this convergence was greater computation times in both cases.

In summary, all three models provide acceptable results in locations away from the endplates. Thick shell model strains tend to be notably smaller than either the shell or combination model values near the endplates. Results from this end-on explosion test and the one reported by Boticario [Ref. 10] show that hoop stain predictions near the endplates were not significantly greater in magnitude than the experimental results. Thus, the Belytschko/Lin/Tsay shell element represents the optimum modeling technique by providing fairly accurate strain predictions with a minimum of computational effort.

B. VARIATIONS IN ATTACK GEOMETRY

The presence of underwater currents or cylinder misalignments in test preparations may have contributed to errors in strain predictions. To determine the sensitivity of the numerical strain predictions to the attack geometry the simulated charge was placed at two different positions along the 15 feet arc from the cylinders. These positions were in

39

the same horizontal plane but at angles of 5.0 and 10.0 degrees from the original end-on and side-on axes. This shift of charge location is equivalent to rotation of the cylinders by 5.0 or 10.0 degrees. Variations in geometry greater than 10.0 degrees were not considered feasible for this analysis.

The sensitivity of the side-on cylinder to rotation was seen to have a minor effect on cylinder response. Illustrations of side-on cylinder rotational sensitivity are shown in Figures 47 through 55. A rotation of 5.0 degrees was seen to have a negligible effect on cylinder response. At a rotation of 10.0 degrees, cylinder response was affected to a noticeable extent at the front (location 1) and back (location 3) positions. The off-axis placement of the charge resulted in a slight range difference between the charge and gage locations A and E. Cylinder rotation was performed such that location A was slightly nearer to the charge than location E. As a result, predicted strain values increased near location A and decreased near location E on the front of the cylinder. The effect of rotation on the back of the cylinder was primarily to disperse the strain in a more uniform manner. The relatively large strain area near the ring-stiffener was no longer visible. As a result, strain magnitudes in the back of the rotated cylinder were lower than in the zero degrees rotation case. Overall, the presence of side-on cylinder rotations did not adequately account for quantitative differences between numerical and experimental results.

The test set-up provided in this experiment was partially chosen to examine the presumed symmetry of response at locations A1 and E1. An examination of the experimental data showed that response to the compressive shock wave began 0.115

40

milliseconds later at location E1 than at location A1. Under the assumption of a spherical shock wave, a cylinder rotation of 12.3 degrees would be required to account for this delay. Since cylinder rotation of this magnitude was unlikely, the spherical wave assumption may not be accurate. Wave front warpage at this range was apparently significant enough to be observed in this test.

A similar cylinder rotation scheme was conducted for end-on cylinder strain values. The cylinder was rotated such that location 3 was slightly closer to the charge than location 1. End-on cylinder response was more sensitive to rotations than the side-on attack geometry. This effect can be seen by comparing Figures 48 and 57. Rotations of 5.0 degrees produced visibly different strain magnitudes in the end-on attack geometry. In both attack geometries, minimal sensitivity to rotation occurred at the top of the cylinder (location 2) as illustrated in Figures 52 and 58. The characteristics of the physical response, such as the oscillation frequency, were nearly identical for all three cases. Results of the end-on cylinder rotations are shown in Figures 56 through 71.
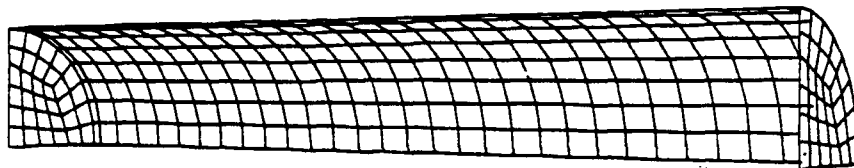
Figure 36. Unstiffened Aluminum Cylinder Quarter Model
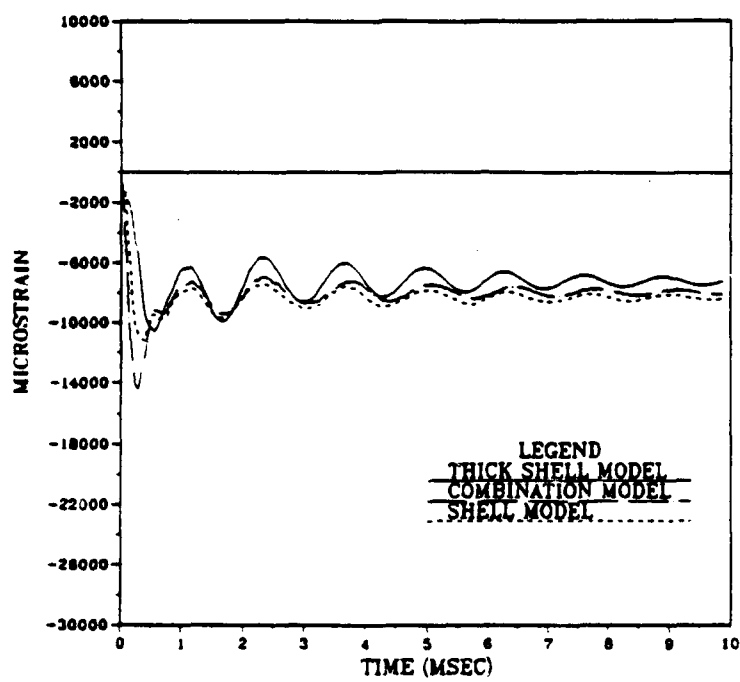
Figure 37. Model Formulation Comparison of Axial Strain
2.9 inches from Near End

42
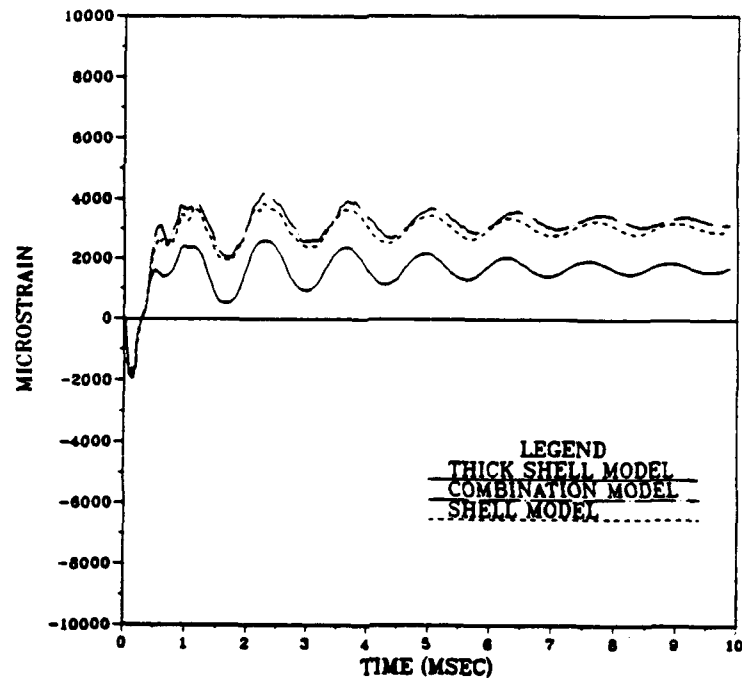
Figure 38. Model Formulation Comparison of Axial Strain
8.5 inches from Near End
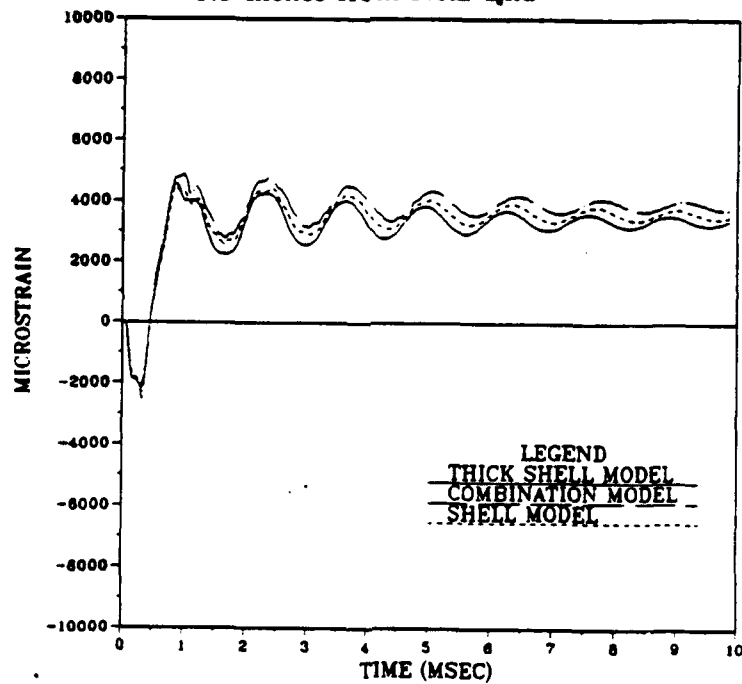
Figure 39. Model Formulation Comparison of Axial Strain
21.0 inches from Near End

43
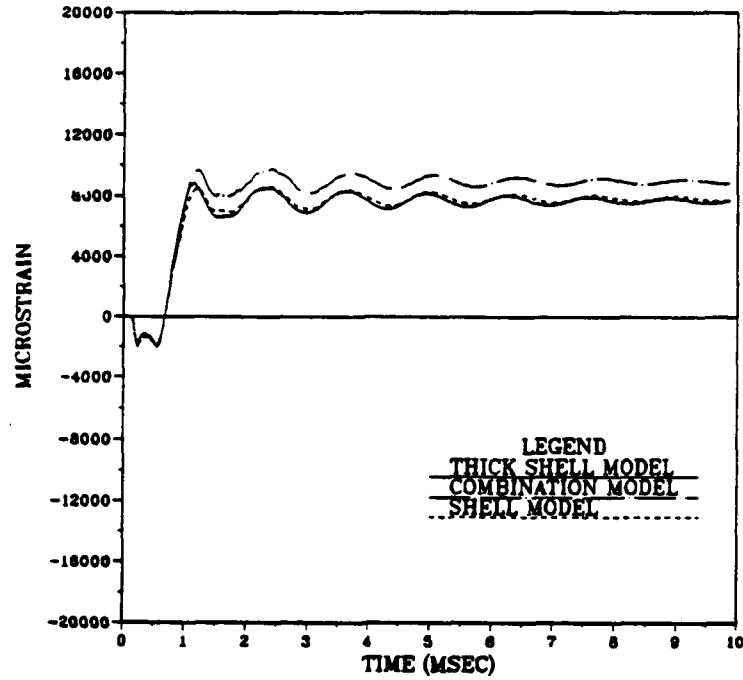
Figure 40. Model Formulation Comparison of Axial Strain 33.5 inches from Near End
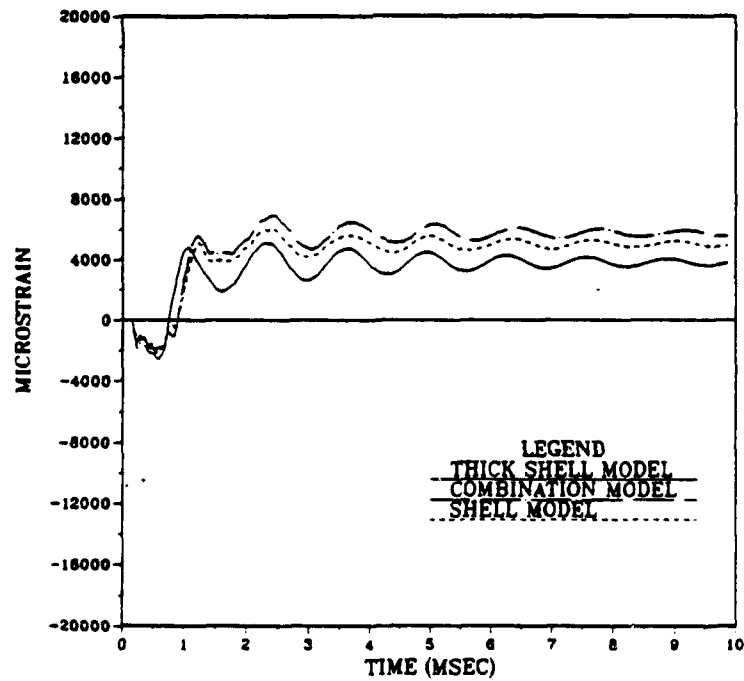
Figure 41. Model Formulation Comparison of Axial Strain 39.1 inches from Near End

44
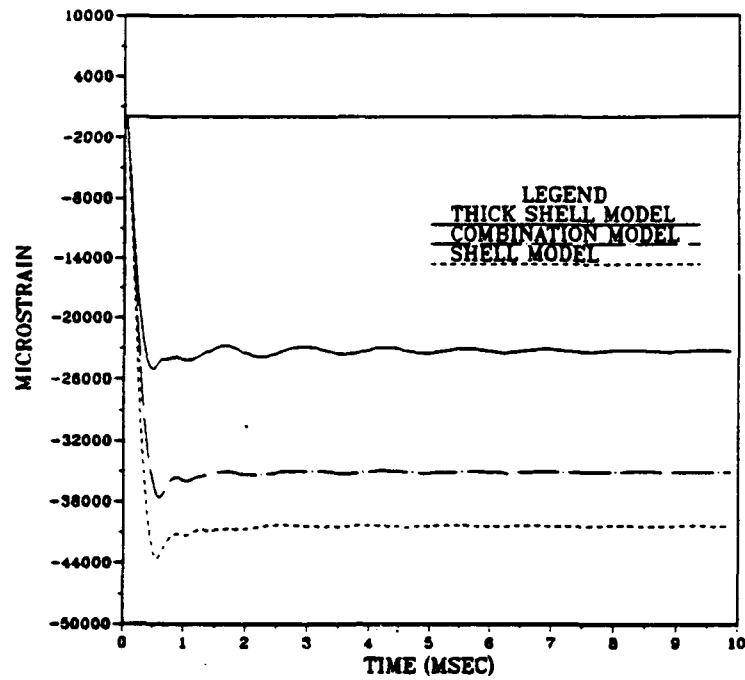
Figure 42. Model Formulation Comparison of Hoop Strain
2.9 inches from Near End
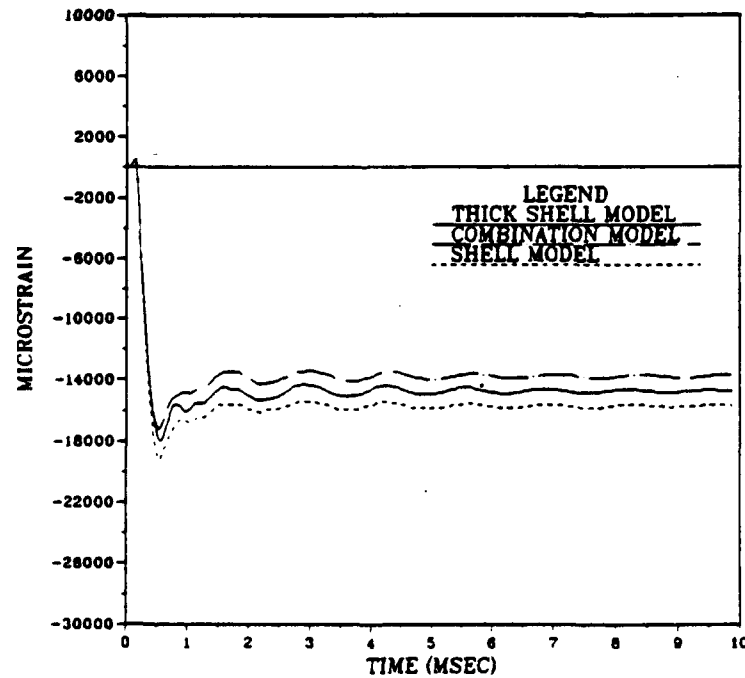
Figure 43. Model Formulation Comparison of Hoop Strain
8.5 inches from Near End
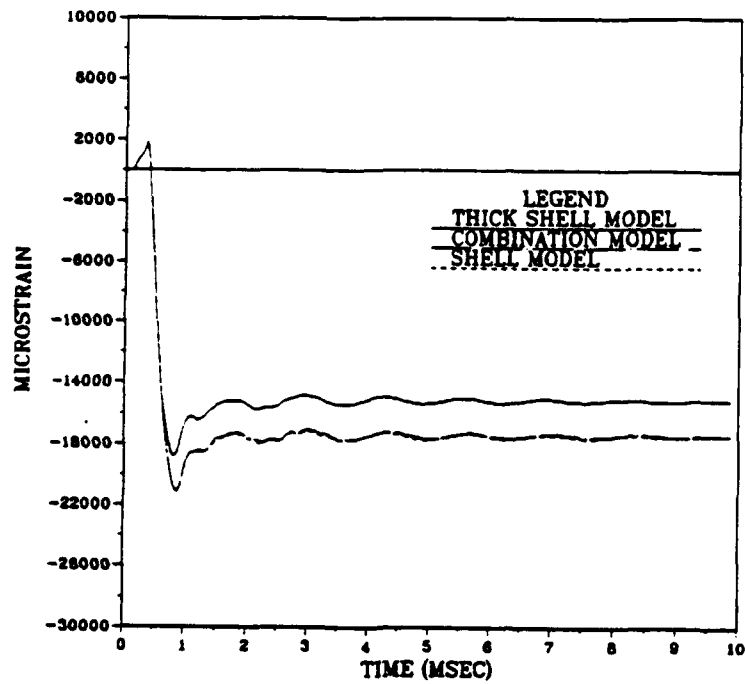
Figure 44. Model Formulation Comparison of Hoop Strain
21.0 inches from Near End
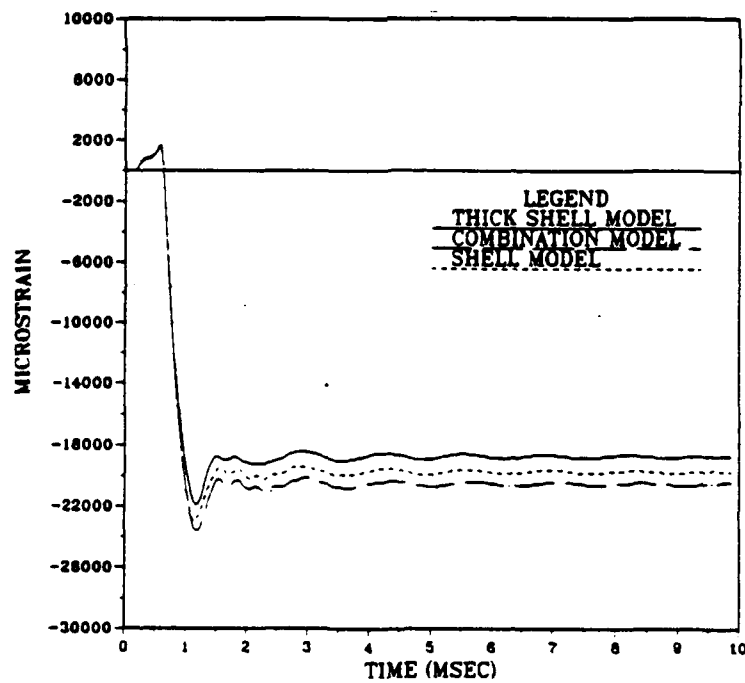
Figure 45. Model Formulation Comparison of Hoop Strain
33.5 inches from Near End
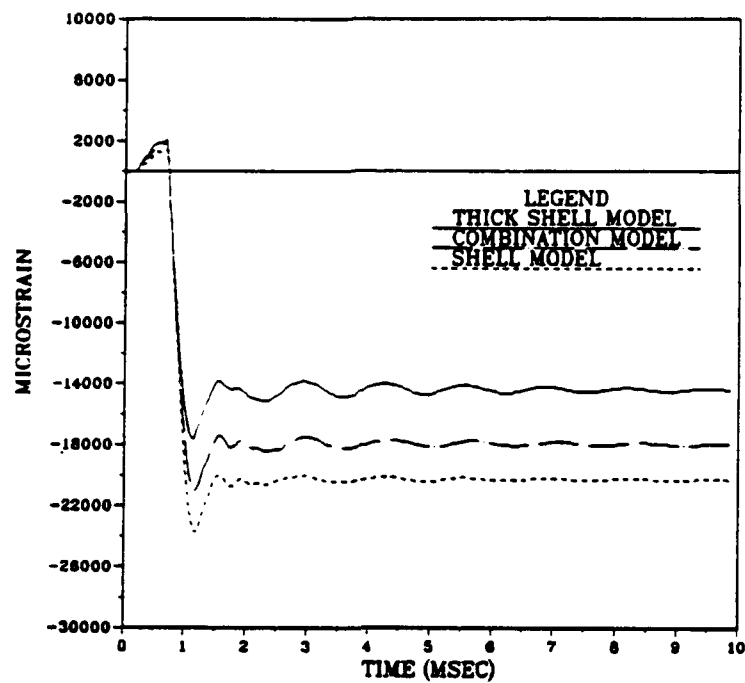
Figure 46. Model Formulation Comparison of Hoop Strain 39.1 inches from Near End
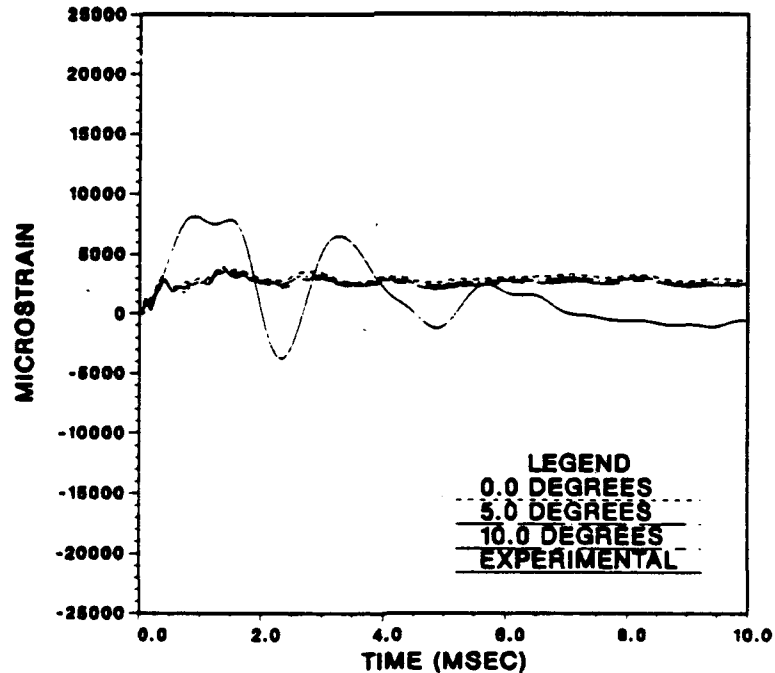
Figure 47. Side-On Cylinder Rotation Sensitivity Results for Axial Strain at Location A2

47
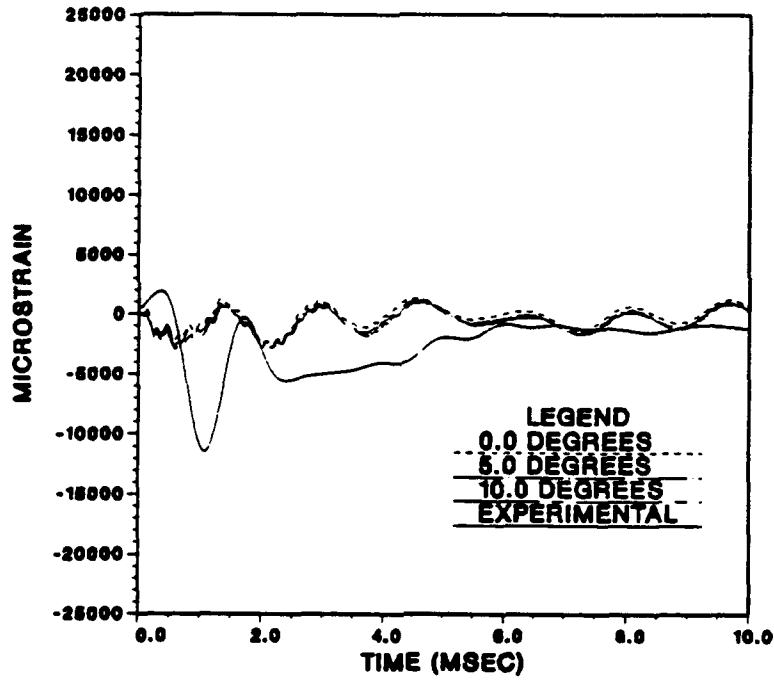
Figure 48. Side-On Cylinder Rotation Sensitivity Results for Axial Strain at Location B1

Figure 49. Side-On Cylinder Rotation Sensitivity Results for Hoop Strain at Location B1

Figure 50. Side-On Cylinder Rotation Sensitivity Results for Axial Strain at Location B3

Figure 51. Side-On Cylinder Rotation Sensitivity Results for Hoop Strain at Location B3

49

Figure 52. Side-On Cylinder Rotation Sensitivity Results
for Axial Strain at Location D2

Figure 53. Side-On Cylinder Rotation Sensitivity Results
for Axial Strain at Location D3

50

Figure 54. Side-On Cylinder Rotation Sensitivity Results for Axial Strain at Location E1

Figure 55. Side-On Cylinder Rotation Sensitivity Results for Hoop Strain at Location E1

51

As in the side-on attack geometry, the variations in strain magnitude due to end-on cylinder rotation did not adequately account for the quantitative differences between the numerical and experimental values. In nearly all cases, an axisymmetric attack geometry with no rotation provided the best comparisons with experimental results.

C. VARIATIONS IN MESH DENSITY

The sensitivity of the numerical strain values to mesh density was investigated by creation of a half-cylinder model with 896 shell elements. This fine mesh model incorporated elements whose longitudinal dimension was about one-half the size of the coarse model elements. The fine mesh model used in this analysis of side-on attack results is shown in Figure 72. Mesh density comparison plots are shown in Figures 73 through 81.

The effect of increasing mesh density was most significant in high strain areas as seen at locations B3 (Figure 77) and E1 (Figure 81). The finer mesh allowed for larger strain gradients near the endplates and ring stiffener. A somewhat different strain pattern was observed with the fine mesh model than the coarse mesh model. Hoop strain at location E1 decreased in magnitude while hoop strain at location B3 increased in magnitude with the fine mesh model. This difference suggests the greatest compressive hoop strain in the locations shown should occur near the ring stiffener on the back side of the cylinder.

Strain values with the fine mesh model in the low strain areas were comparable to coarse mesh strain values as seen at locations A2 (Figure 73), B1 (Figures 74 and 75),

and D2 (Figure 78). The differences between the two models were small enough that a fine mesh model would not be desirable due to the additional time required for computations.

The most efficient and accurate model would have a somewhat finer mesh near the endplates and ring stiffener than was developed in the coarse mesh model. The increased computational time would then be offset by improvements in accuracy in the high strain areas.
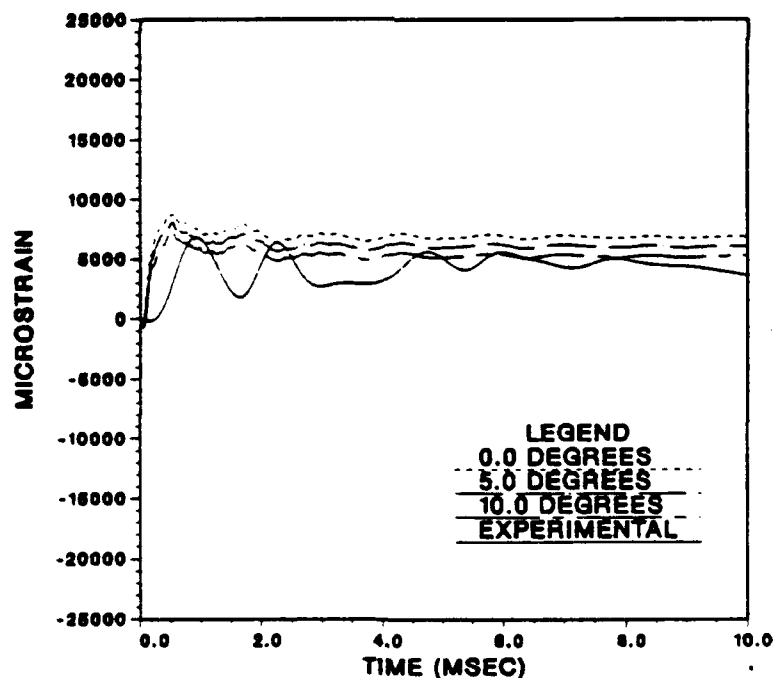
Figure 56. End-On Cylinder Rotation Sensitivity Results for Axial Strain at Location A1
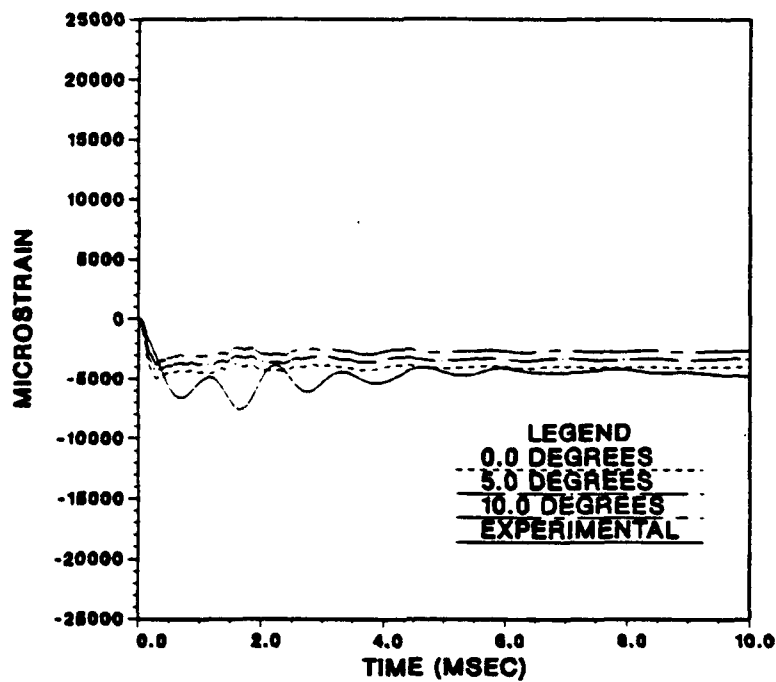
Figure 57. End-On Cylinder Rotation Sensitivity Results for Hoop Strain at Location A1
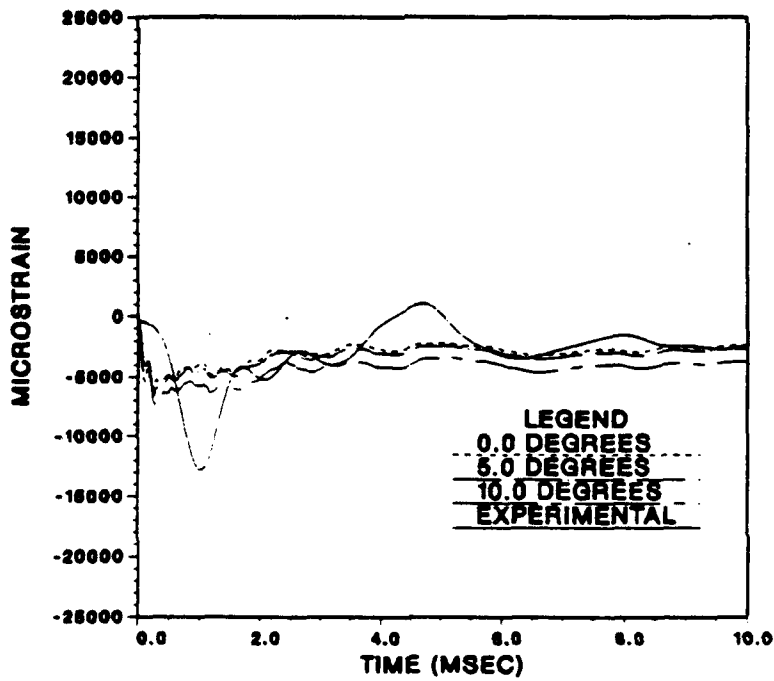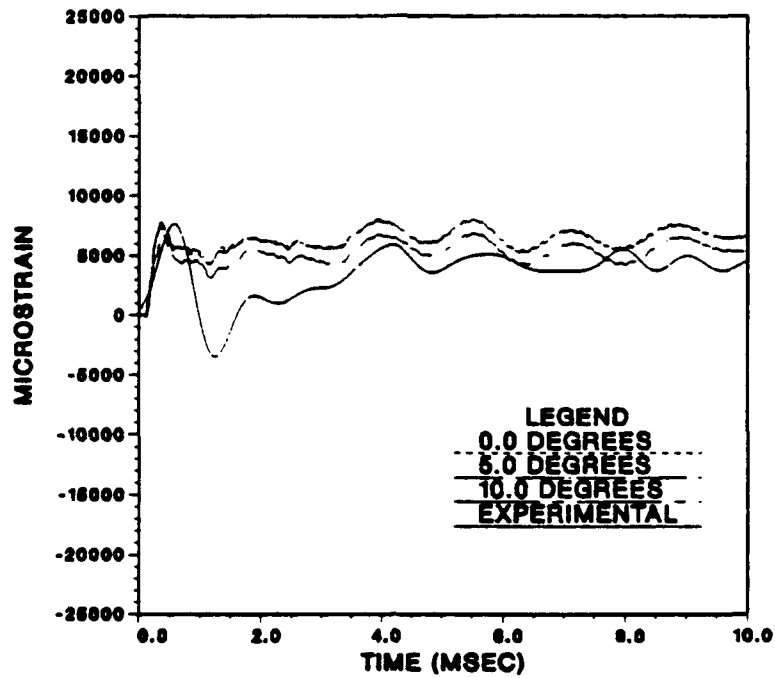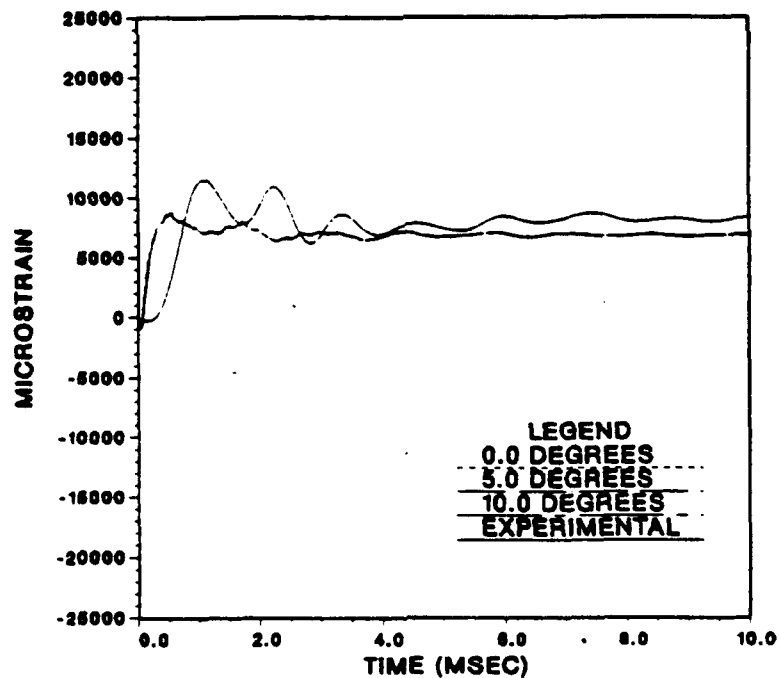

Figure 58. End-On Cylinder Rotation Sensitivity Results for Axial Strain at Location A2
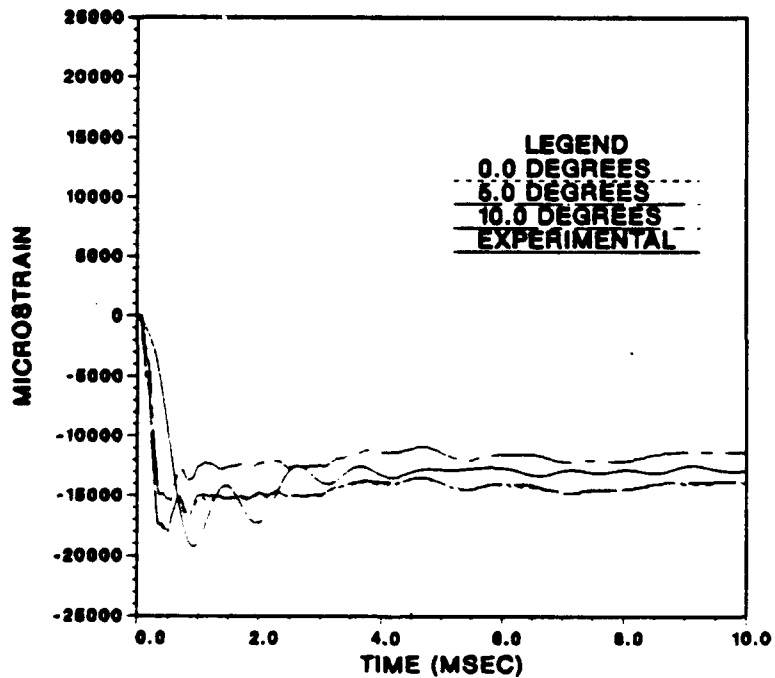
54
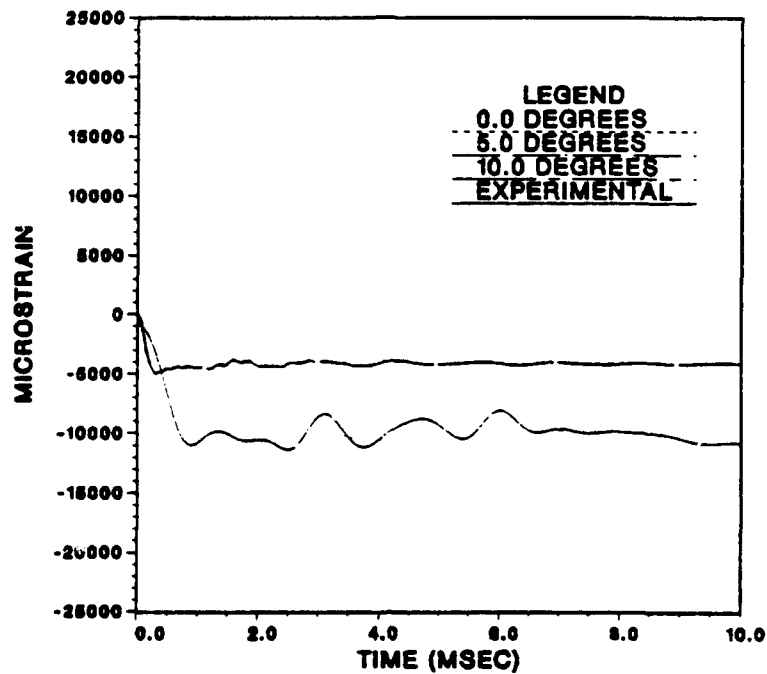
Figure 59. End-On Cylinder Rotation Sensitivity Results for Hoop Strain at Location A2
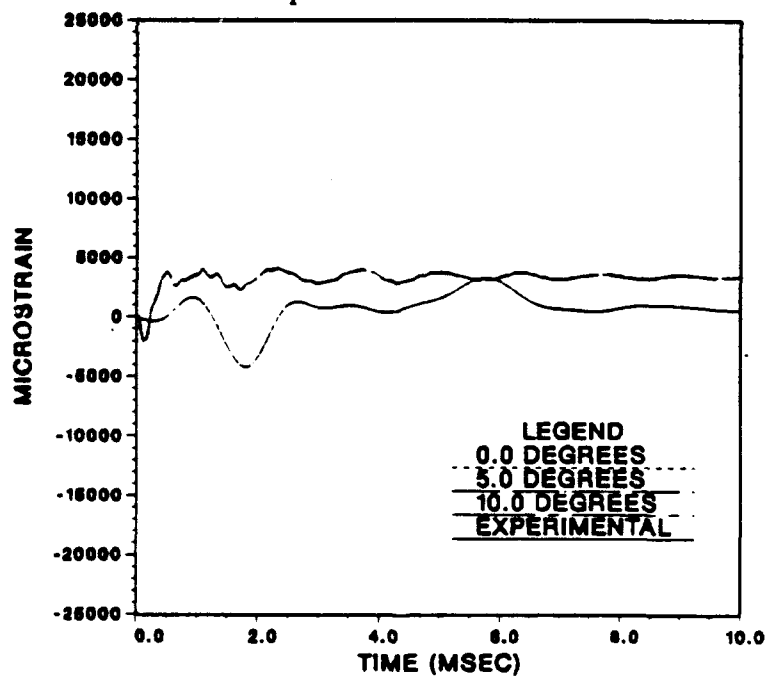
Figure 60. End-On Cylinder Rotation Sensitivity Results for Axial Strain at Location B2
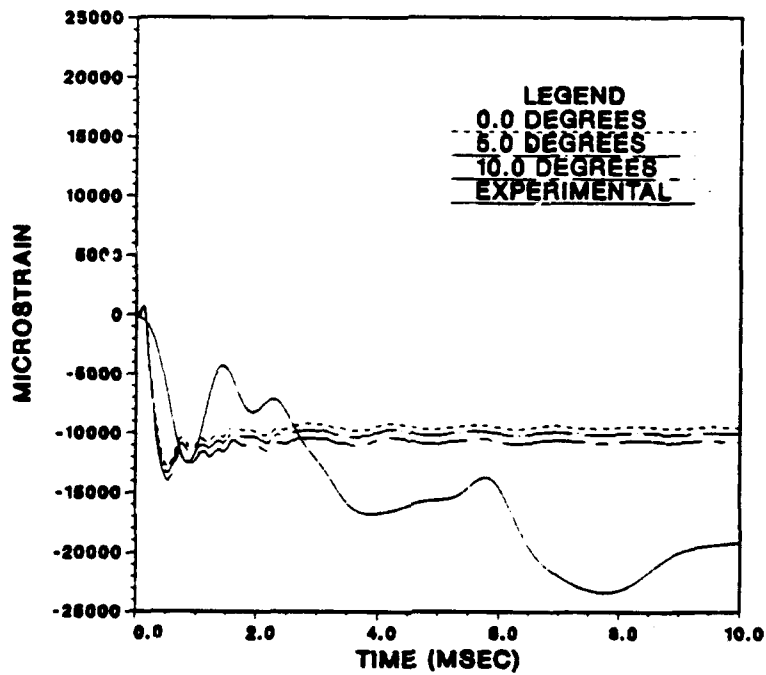
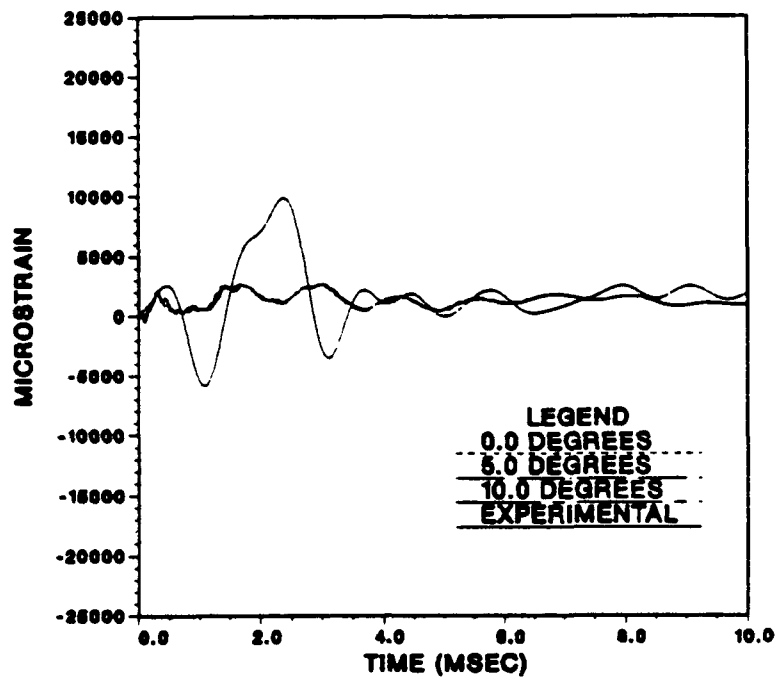**Figure 61.** End-On Cylinder Rotation Sensitivity Results for Hoop Strain at Location B3
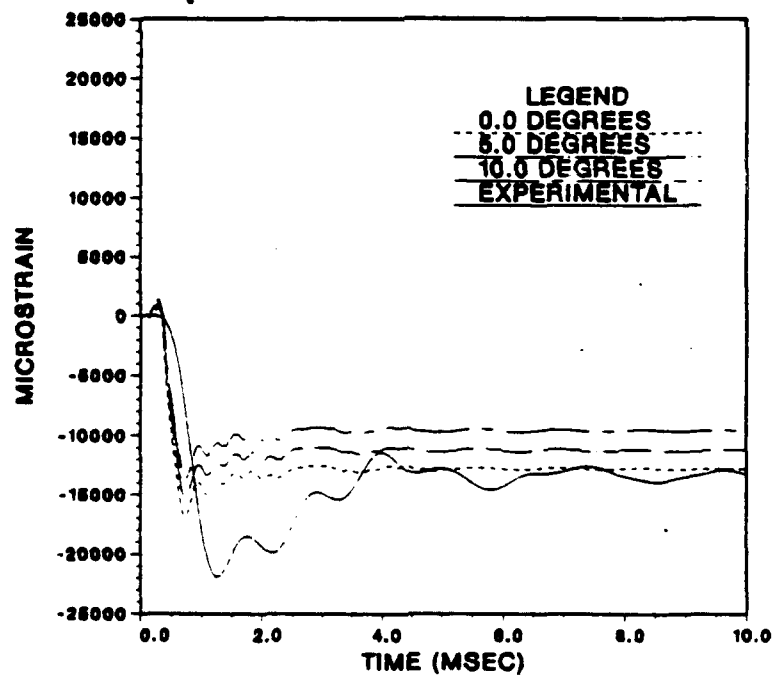
Figure 62. End-On Cylinder Rotation Sensitivity Results for Hoop Strain at Location C1
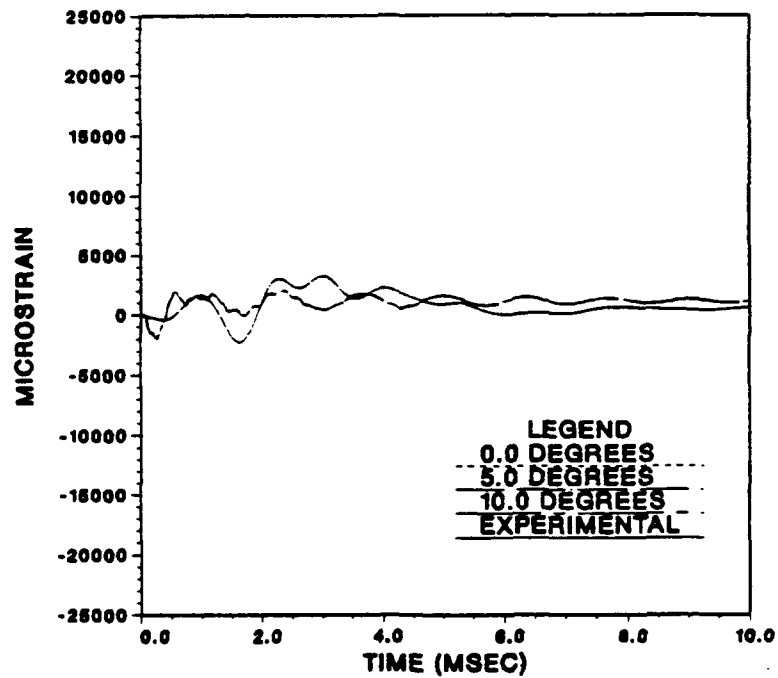
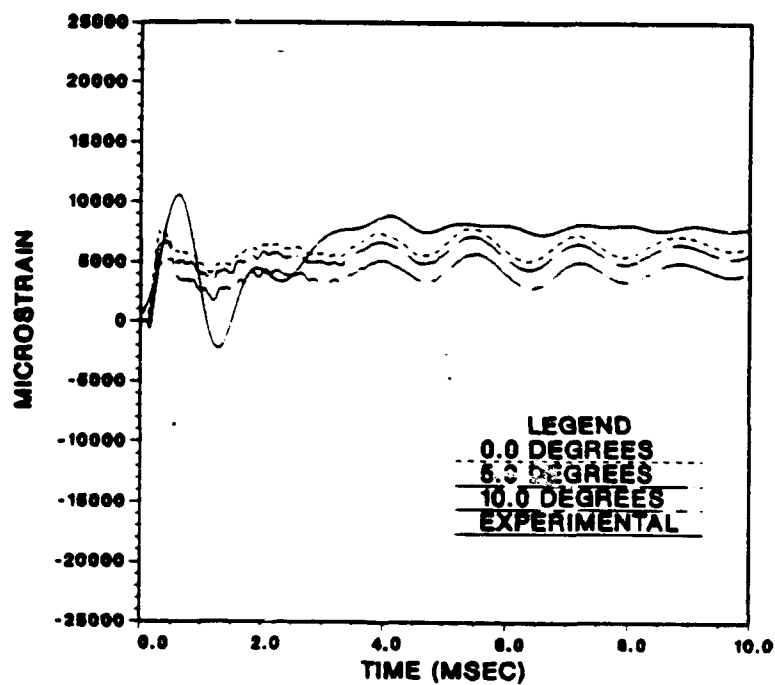**Figure 63.** End-On Cylinder Rotation Sensitivity Results for Axial Strain at Location C2
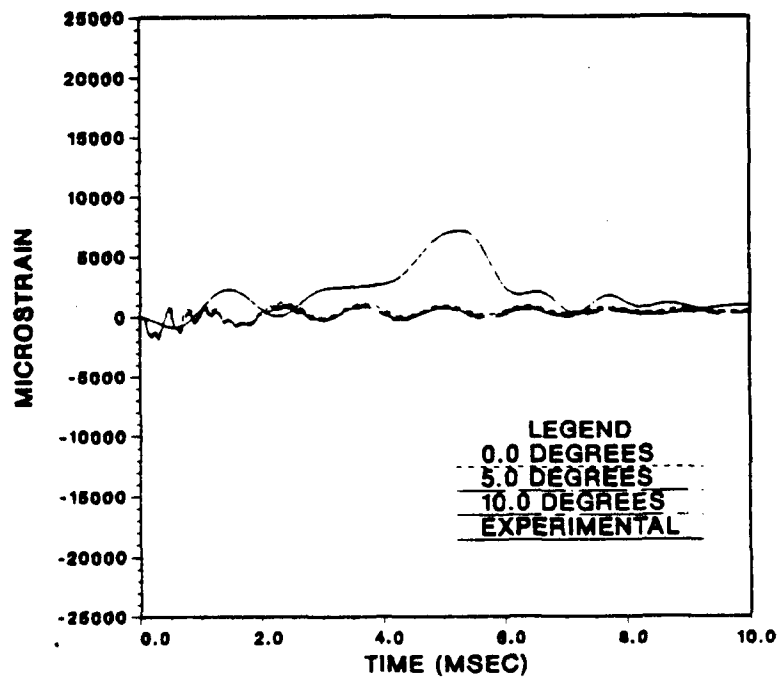
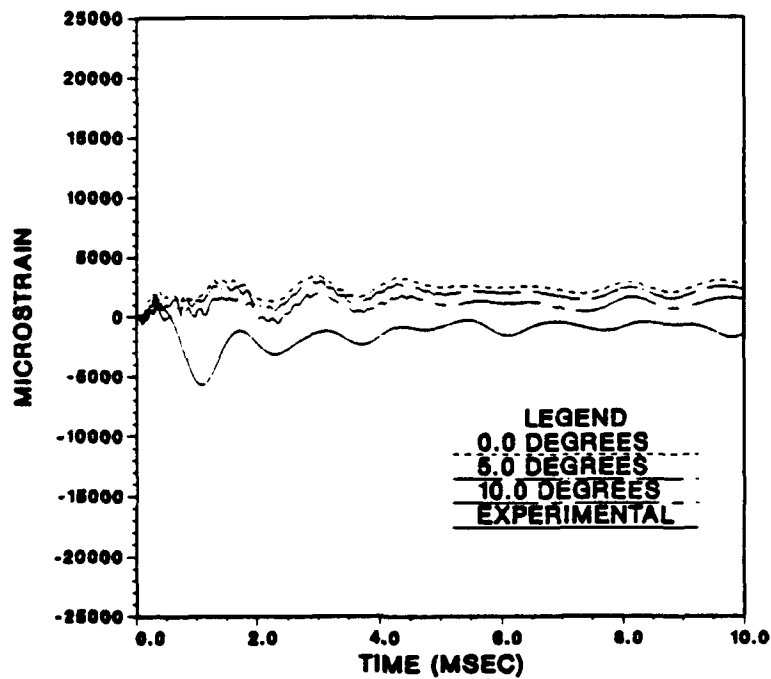**Figure 64.** End-On Cylinder Rotation Sensitivity Results for Axial Strain at Location D3
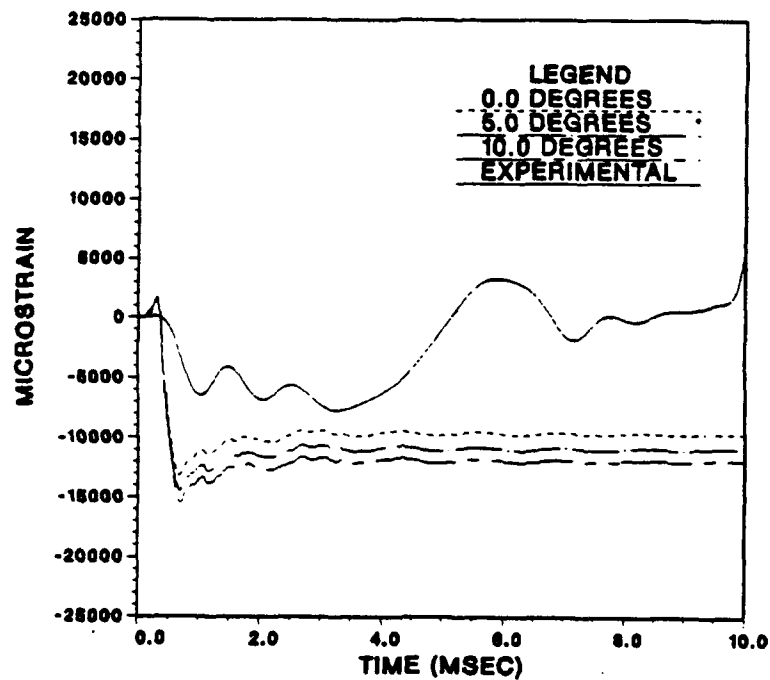
Figure 65. End-On Cylinder Rotation Sensitivity Results for Hoop Strain at Location D3
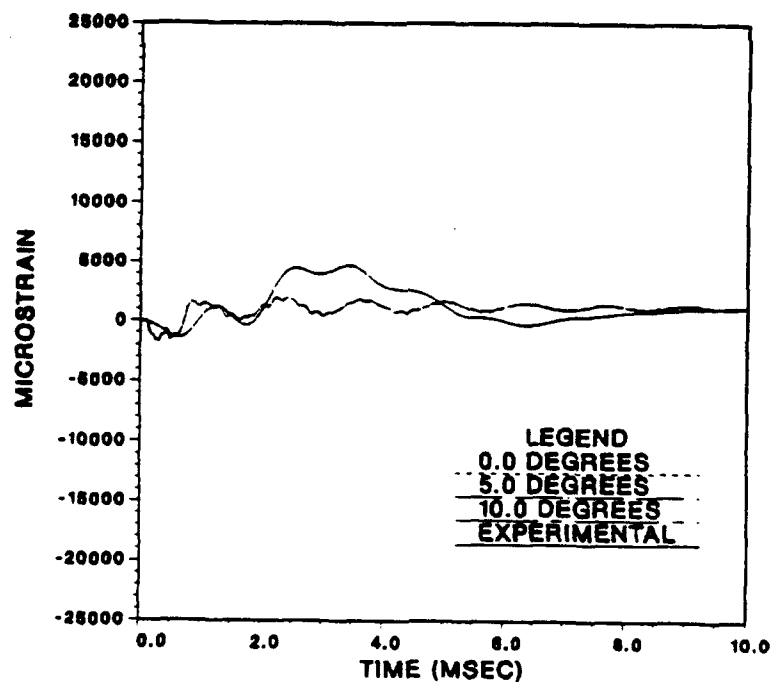
Figure 66. End-On Cylinder Rotation Sensitivity Results for Axial Strain at Location E2
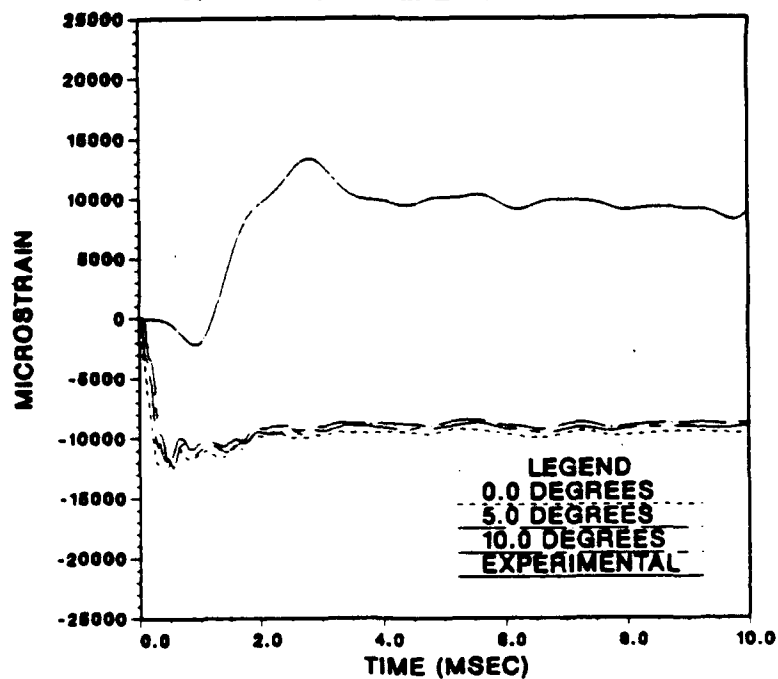
58
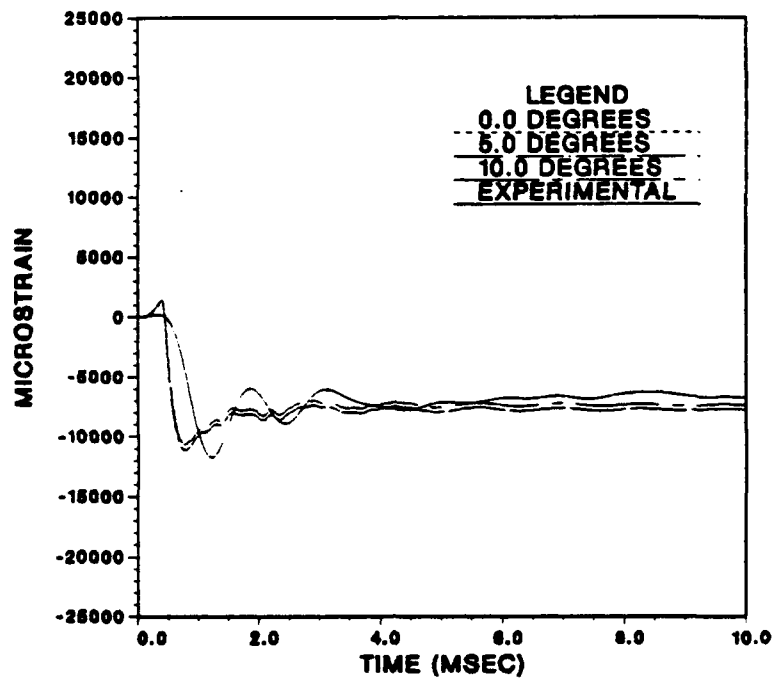
Figure 67. End-On Cylinder Rotation Sensitivity Results for Hoop Strain at Location E2
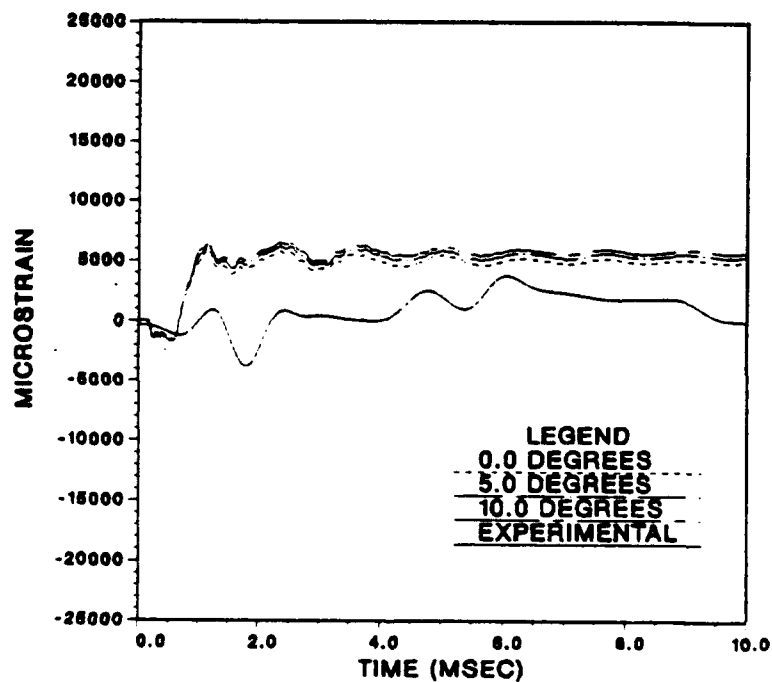
Figure 68. End-On Cylinder Rotation Sensitivity Results for Axial Strain at Location F1

59
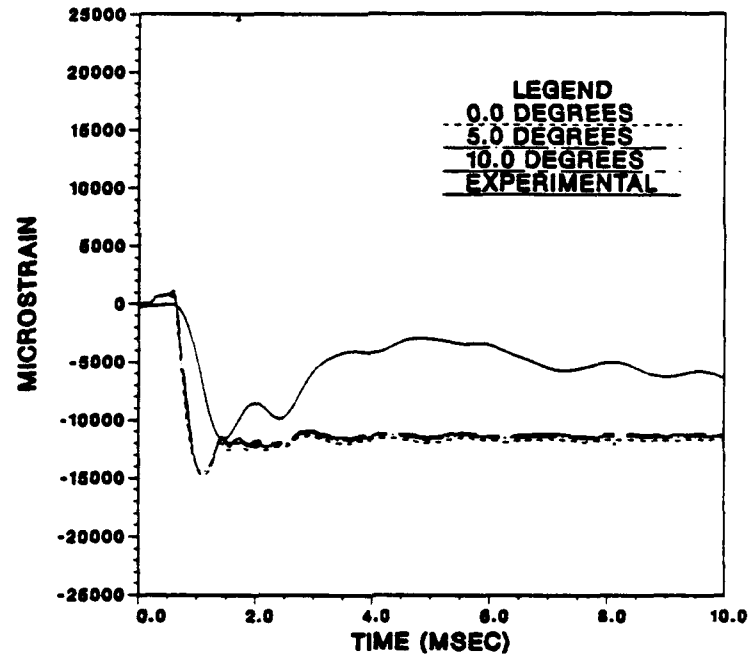
Figure 69. End-On Cylinder Rotation Sensitivity Results for Hoop Strain at Location F1
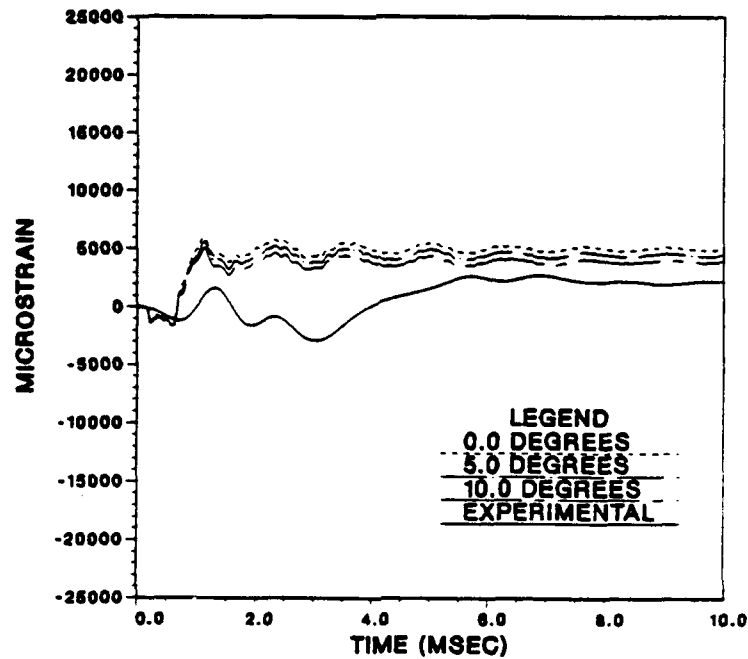
Figure 70. End-On Cylinder Rotation Sensitivity Results for Axial Strain at Location F3

60
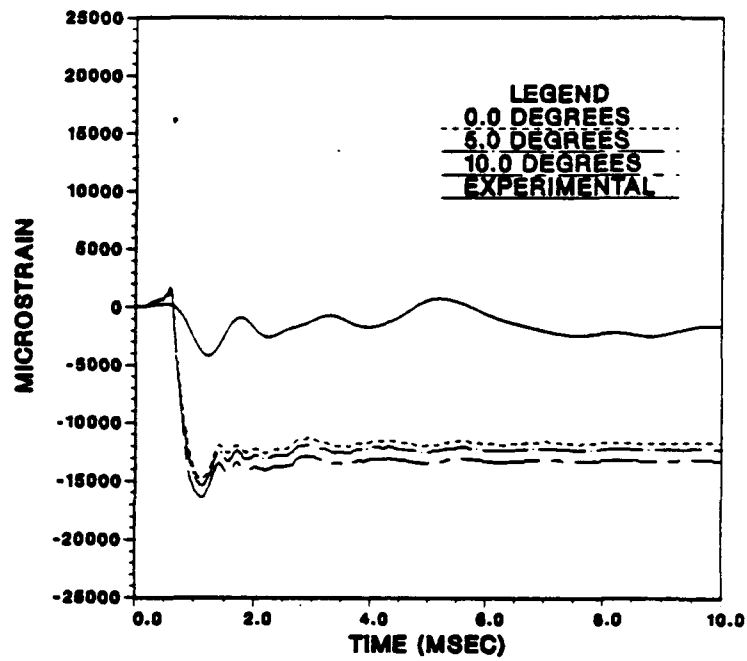
Figure 71. End-On Cylinder Rotation Sensitivity Results
for Hoop Strain at Location F3
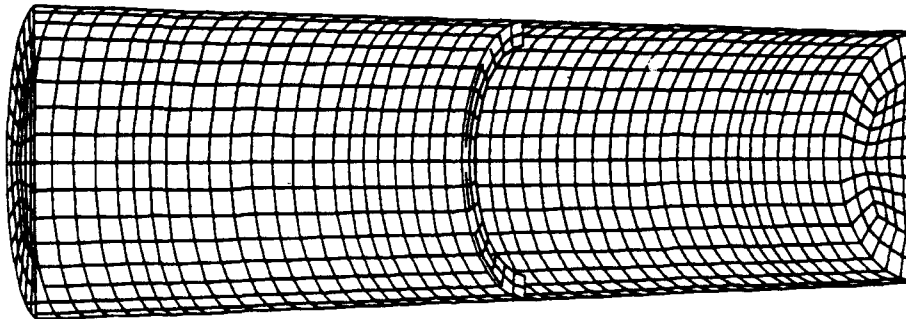
Figure 72. Half-Cylinder Fine Mesh Model

61
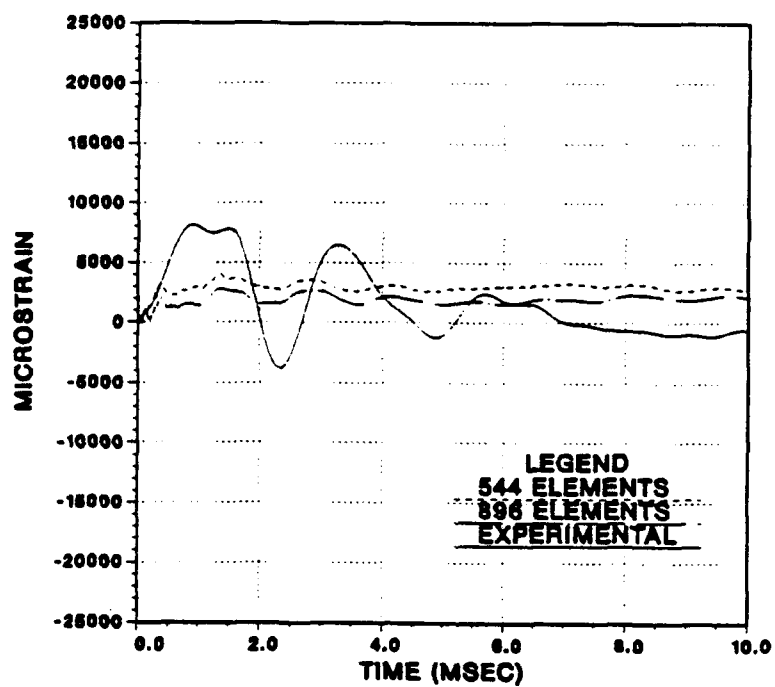
Figure 73. Effect of Mesh Density for Side-On Geometry Axial Strain at Location A2
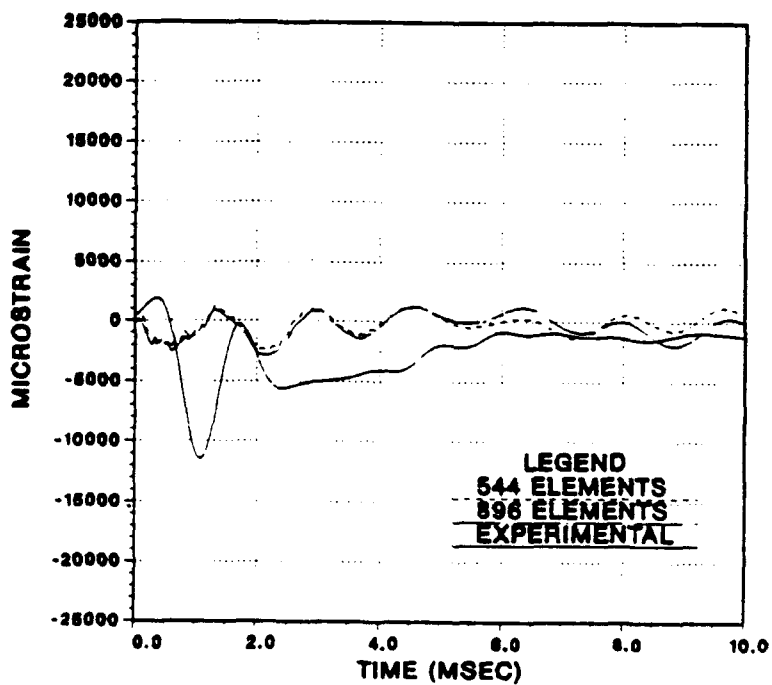
Figure 74. Effect of Mesh Density for Side-On Geometry Axial Strain at Location B1

62
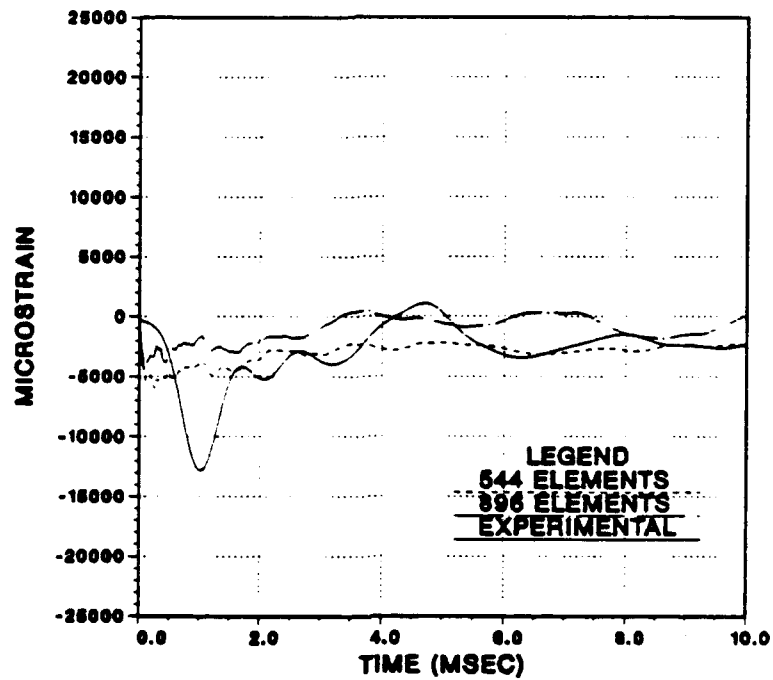
Figure 75. Effect of Mesh Density for Side-On Geometry
Hoop Strain at Location B1
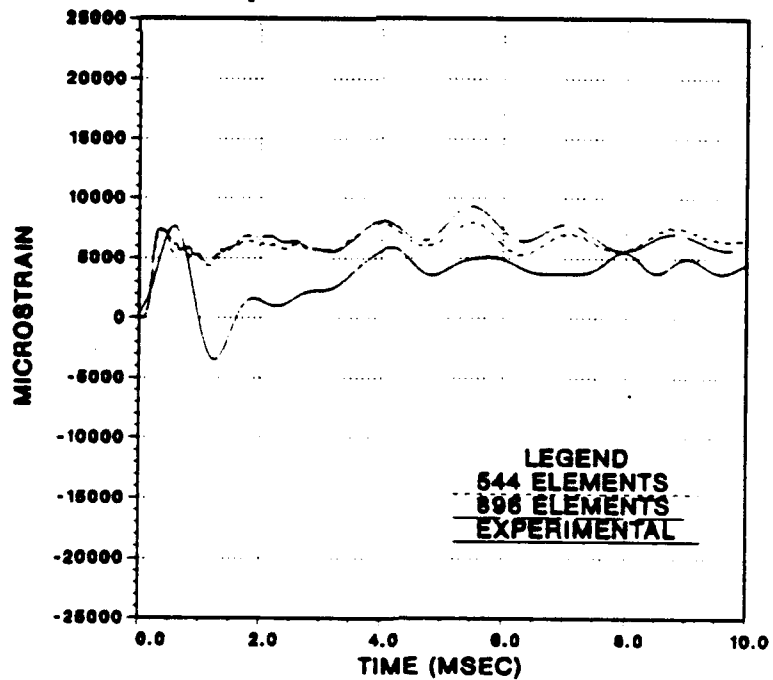
Figure 76. Effect of Mesh Density for Side-On Geometry
Axial Strain at Location B3

63
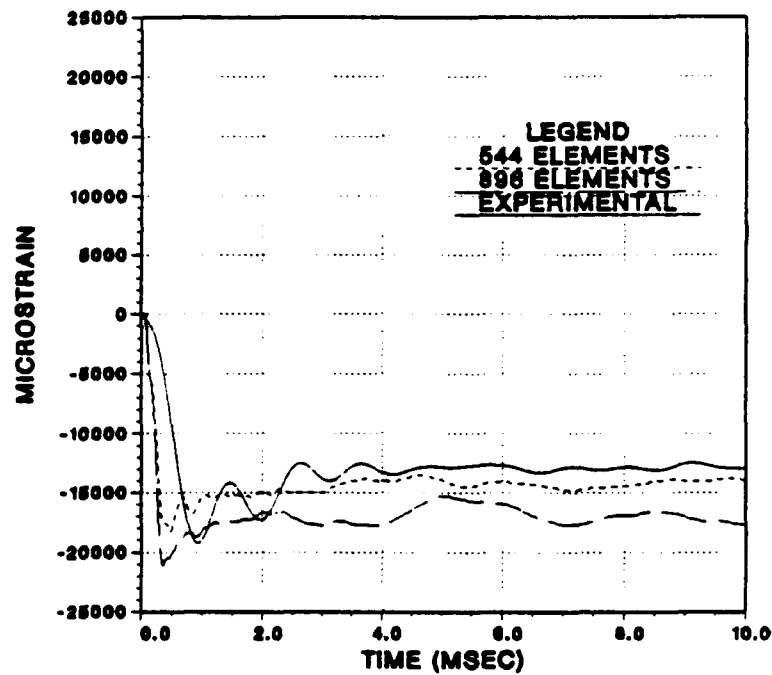
Figure 77. Effect of Mesh Density for Side-On Geometry
Hoop Strain at Location B3
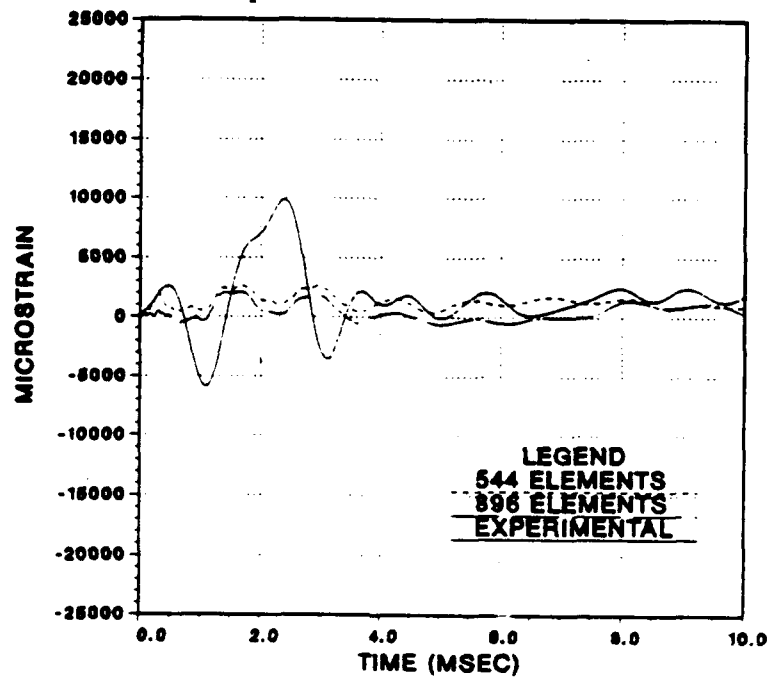
Figure 78. Effect of Mesh Density for Side-On Geometry
Axial Strain at Location D2
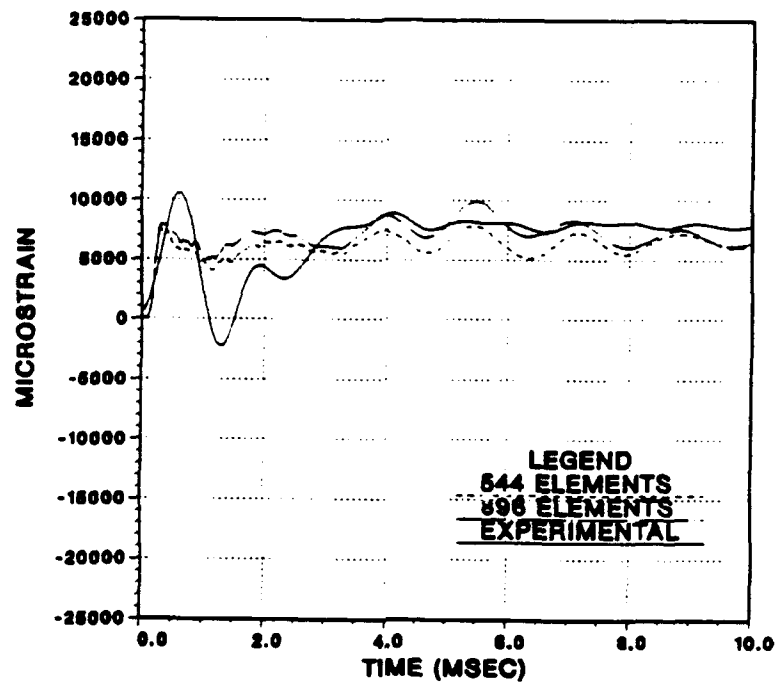
Figure 79. Effect of Mesh Density for Side-On Geometry
Axial Strain at Location D3
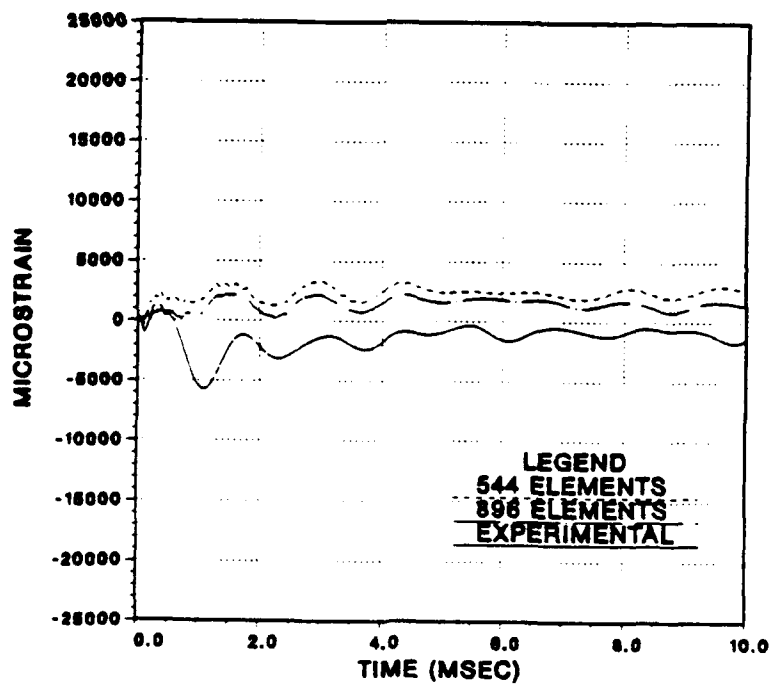
Figure 80. Effect of Mesh Density for Side-On Geometry
Axial Strain at Location E1

65
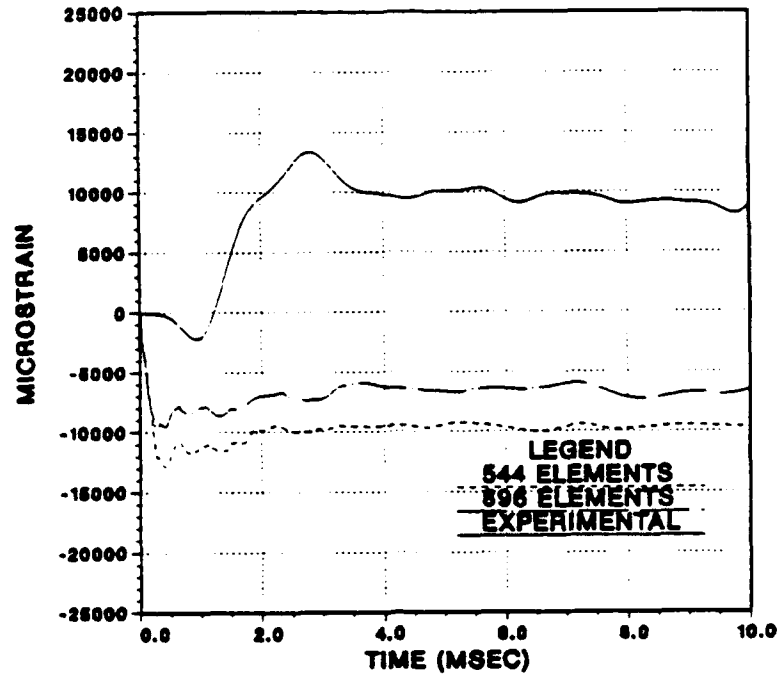
Figure 81. Effect of Mesh Density for Side-On Geometry
Hoop Strain at Location E1

66

IV. FAILURE ANALYSIS

The analysis conducted thus far has attempted to explain the experimental results with numerical predictions from models which did not employ failure criteria. The numerical predictions near visible failure zones were in poor agreement with experimental results from both cylinders. A material model which incorporated a failure criteria for effective plastic strain was studied to improve upon strain predictions in these areas. Since end-on cylinder integrity was lost due to weld failure, only the side-on cylinder response will be discussed in this section.

The elastic-plastic model used in this analysis calculated plastic strain values in the same manner as the model without failure criteria. As discussed in [Ref. 11], deviatoric stresses are updated elastically for each succeeding time step by the relation:

$$\sigma^* = \sigma^n + C\Delta\varepsilon \qquad (7)$$

where σ^* is the trial stress tensor, σ^n is the stress tensor from the previous time step, C is the tangent modulus matrix and $\Delta\varepsilon$ is the incremental strain tensor. If the yield stress is not exceeded, the trial stress is utilized in the following time step. If the yield stress is exceeded, an increment of plastic strain is computed and the stresses are reduced to the yield stress. In addition, if the effective plastic strain value at failure is exceeded, the element loses its load bearing capability and the effective (von Mises) stress is reduced to zero.

The use of the incremental plastic stress-strain relations in this manner accurately represents a material with perfectly plastic behavior. Since 6061-T6 aluminum is fairly insensitive to strain rate effects at these test conditions, this perfectly plastic approximation is a reasonable one.

The model chosen for this failure analysis consisted of the same ring-stiffened half cylinder model which contained 544 surface elements. An effective plastic strain at failure of 4 percent (40,000 microstrain) was used in order to be below the static tensile failure strain value of 7 percent yet well above the 0.2 percent offset yield point.

An examination of experimental strain values for the side-on attack geometry reveals that the greatest strain magnitudes occurred on the front and back locations of the cylinder. Specifically, locations near the endplates on the front of the cylinder and the ring stiffener on the back of the cylinder displayed maximum strain values. Thus, the observed fractures in the comparatively low strain area at the top of the cylinder were an unexpected result.

To more accurately model cylinder susceptibility to fractures at the top of the cylinder, the thickness of eight elements was reduced to 86% of the nominal value. This reduction in element thickness was imposed to simulate material property and geometric imperfections in this region. Thus, imperfections near the top of the cylinder were presumed to be the cause of the observed failures. The presence of stress concentrations near this imperfection area would then cause initial failures at the top of the cylinder.

The eight elements chosen for this thickness reduction are shown in Figure 82. These elements are located symmetrically about the ring stiffener. The length of each of

these imperfection zones was about 6.2 inches. The imperfection zone was located slightly behind but adjacent to the element row which contained four strain gages. This geometry was chosen to coincide with the size and location of the actual failure zones.

The response of the cylinder to these imperfection zones was sensitive to the amount of element thickness reduction. A comparison of these thickness values is shown in Figure 83. A reduction in thickness to 90% of the nominal value had a negligible effect on the strain pattern at the top of the cylinder. Failures in the cylinder were not observed for this case. A reduction to 86% of nominal element thickness produced a significant strain pattern variation compared to the 90% nominal thickness case. The deformations are seen to be symmetric about the ring stiffener. An imperfection zone simulated by elements at 80% nominal thickness shows even more severe deformations at the top of the cylinder. However, the large stress concentrations in the vicinity of the failure zone in this case resulted in a global failure of the cylinder within 5 milliseconds of shock wave arrival. Of these three cases, the choice of imperfection zone elements at 86% nominal thickness results in best agreement with experimental results.

The use of this failure model for the side-on attack geometry produced improvements in strain predictions near the failure zone. Unfortunately, the close proximity of the strain gages to these failures resulted in large strain rates and strain magnitudes which prevented collection of valid experimental data for 10 milliseconds.

■   **0.86 * NOMINAL THICKNESS ELEMENTS**
(0.215 IN.)

⊠   **STRAIN GAGE LOCATIONS**
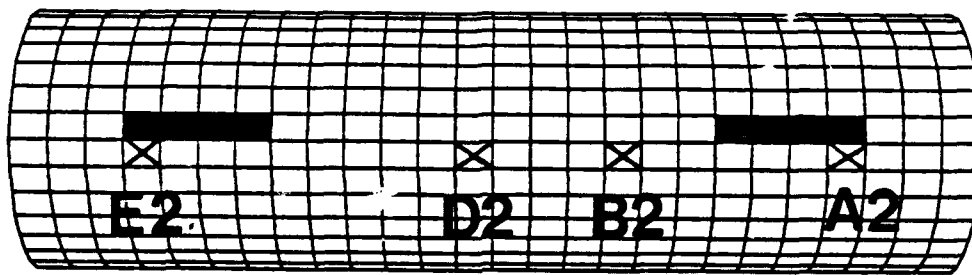
Figure 82. Half-Cylinder Failure Model Top View
(Dark Elements 86% Nominal Thickness)

A plot of axial strain at location B2 is shown in Figure 84. Unfiltered experimental data values indicated that the axial strain magnitude was pro ably saturated at about 2.0 milliseconds. Thus, the maximum strain magnitude at this gage location would be in excess of the values shown in Figure 84 at times beyond 2.0 milliseconds. Nevertheless, the use of failure criteria produced improved qualitative results at early times compared to the original model without failure criteria.

0.9 * nominal thickness elements
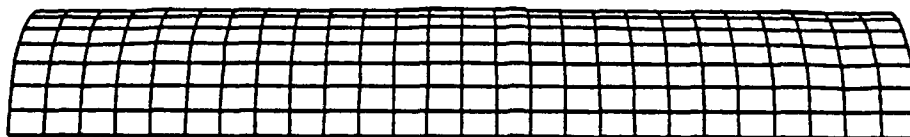
0.86 * nominal thickness elements
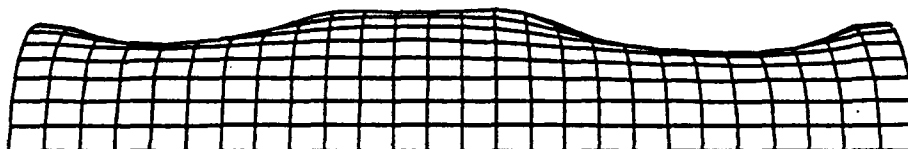
0.80 * nominal thickness elements
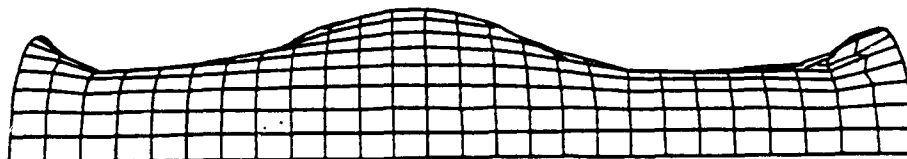
Figure 83. Cylinder Response for Various Imperfection
Element Thicknesses (Frontal View)

71

In a similar manner, numerical results with the failure model at location B2 more accurately predicted the experimental hoop strain response as shown in Figure 85. This strain gage probably failed at about 1.0 millisecond based upon the unfiltered experimental data so strain values after this time are not considered reliable. However, the improvement in the early time response is still significant.

Improvements in numerical strain predictions at gage location D3 were less significant as shown in Figures 86 and 87. Both numerical models poorly predicted the transient behavior of the cylinder but provided a reasonably good estimate of the actual strain values near 5.0 milliseconds. The close proximity of the ring stiffener to location D3 may account for the large strain variations observed in the experimental results.

The use of this failure model has several limitations associated with the post-processor data presentation. First, the strain time history plots can be misleading since a plot continues to be generated even after the element has reached the failure strain criteria. Thus, reference to the effective stress time history is necessary to ensure element strain data is valid. Secondly, the effective plastic strain plot continues to display a strain value after reaching the failure strain. Thus, it is difficult to tell from this plot alone if failure has occurred. Finally, the illustration of the cylinder deformations does not adequately show the presence of failures. Thus, the extent of crack propagation cannot be easily seen in post-processor displays.
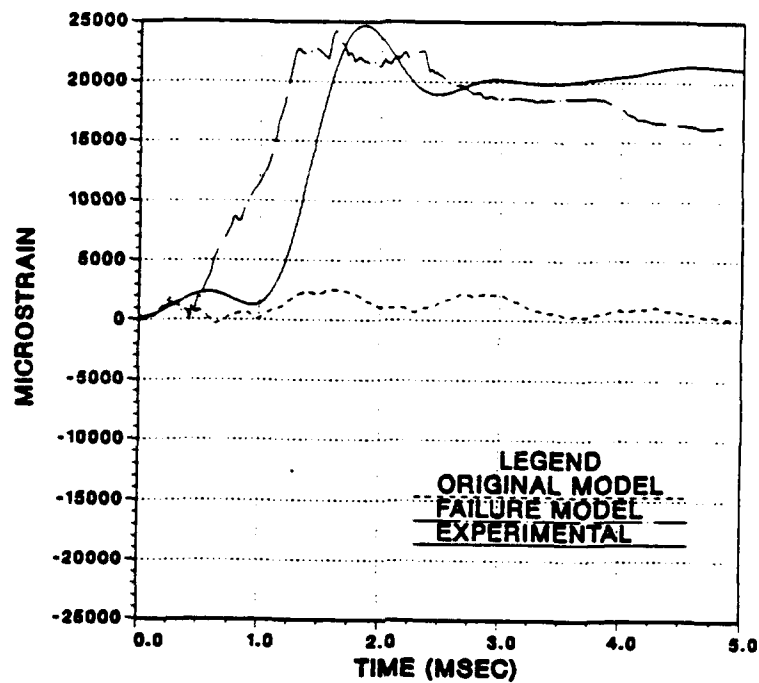
Figure 84. Side-On Explosion Axial Strain at
Gage Location B2 with Failure Criteria.
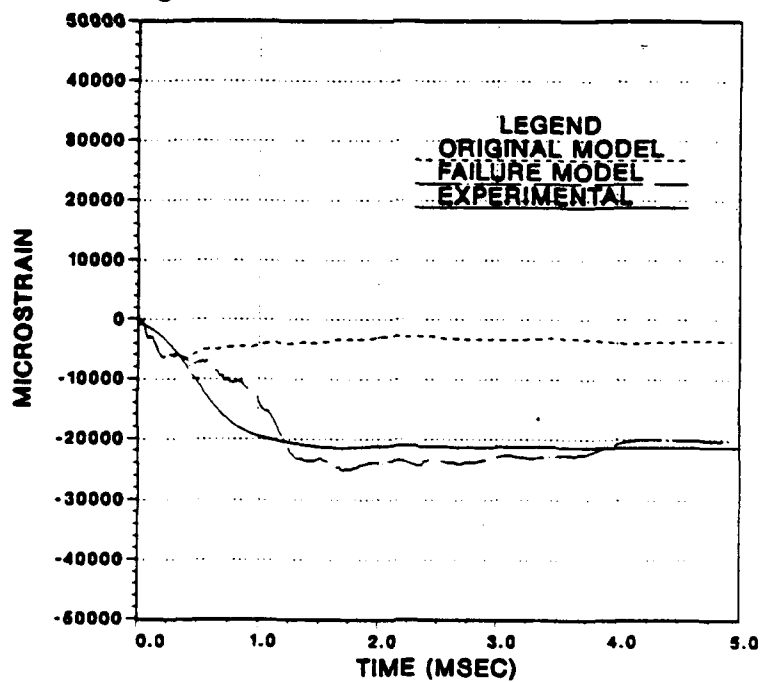
Figure 85. Side-On Explosion Hoop Strain at
Gage Location B2 with Failure Criteria.
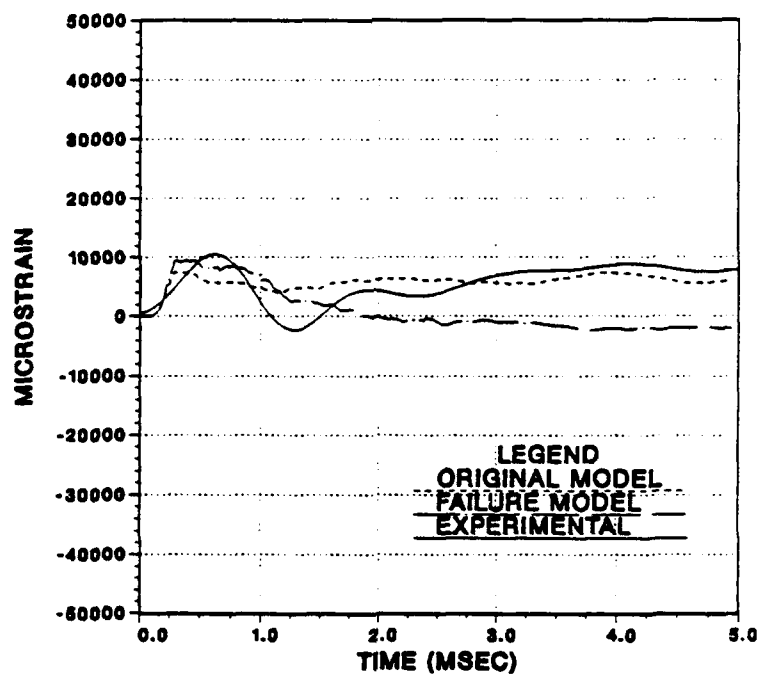
Figure 86. Side-On Explosion Axial Strain at
Gage Location D3 with Failure Criteria.
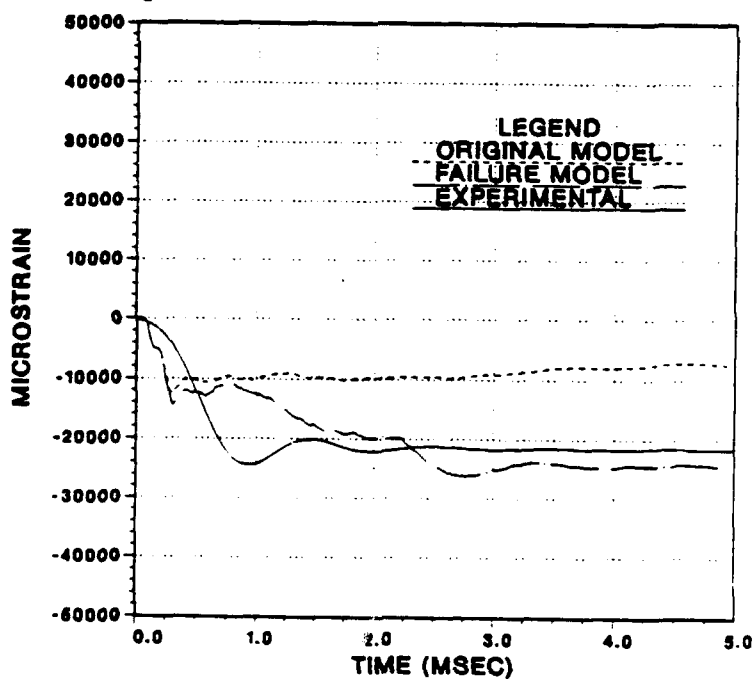
Figure 87. Side-On Explosion Hoop Strain at
Gage Location D3 with Failure Criteria.

74

The application of this failure model to areas adjacent to the imperfection site should also be done with care. The complex dynamic behavior of a structure near a crack is influenced by several microscopic level parameters which cannot easily be measured before testing. A qualitative prediction in this area until the time of failure seems to be the best attainable from this model.

The response of the cylinder adjacent to an imperfection site is shown for gage location A2 in Figures 88 and 89. Axial strain at location A2 (Figure 88) rapidly rises to the strain gage response limit of 50,000 microstrain within 1.5 milliseconds. Since even the static failure strain value for 6061-T6 aluminum is only about 70,000 microstrain, material failure at this location would soon occur. The hoop strain results (Figure 89) show a better comparison with experimental results up until 1.5 milliseconds due to nearby failures. The severe increases in strain at this location are attributable to stress redistribution following the failures in adjacent imperfection zone elements at about 0.4 milliseconds.

The structural response to a failure can be best seen from the effective stress plot shown in Figure 90. This plot shows how stresses near a failure are relaxed and redistributed near a crack zone.
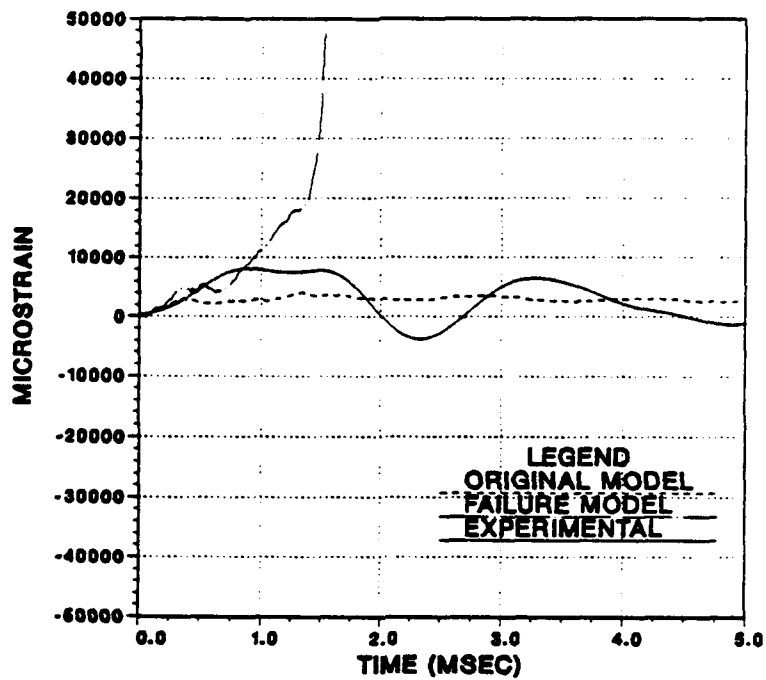
Figure 88. Side-On Explosion Axial Strain at
Gage Location A2 with Failure Criteria.
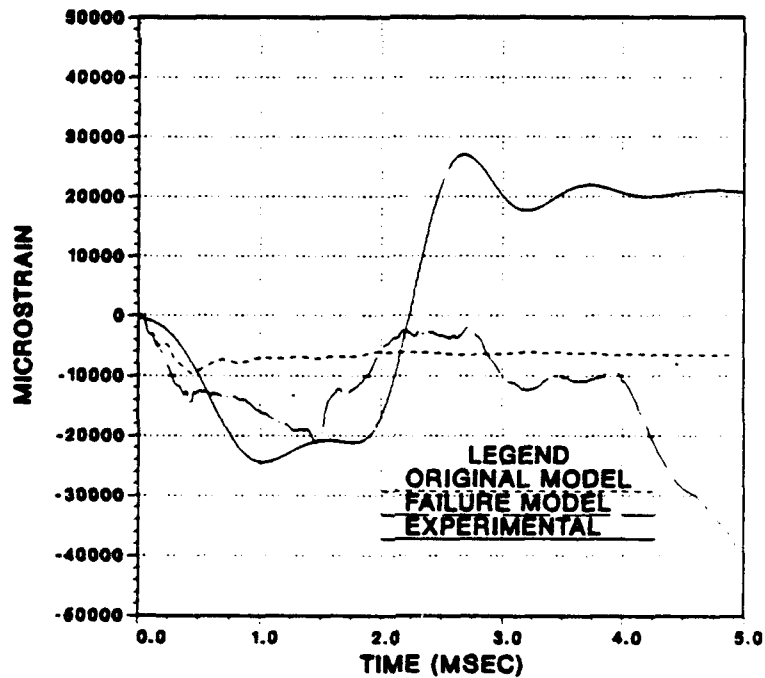
Figure 89. Side-On Explosion Hoop Strain at
Gage Location A2 with Failure Criteria.

76

At the site of a reduced thickness element, or imperfection zone, the effective stress rapidly rises to the yield stress value of 40,000 psi after arrival of the compressive shock wave. The imperfection site experiences stress concentration due to the reduced thickness. Within 0.4 milliseconds, this element undergoes enough plastic strain to reach the failure value. The effective stress drops to zero as the element loses its capability to carry load due to the creation of a free surface at the crack location.

At 0.75 inches from the imperfection site in the circumferential direction, the effective stress again rises to the yield stress value and remains there as the element undergoes plastic strain. This position corresponds to gage location A2. At 0.4 milliseconds, however, this element undergoes a rapid stress reduction as a result of the failure in the adjacent element. This stress relaxation is due to elastic strain recovery. However, since fluid particle pressure is still acting on the cylinder at 0.5 milliseconds, the stress rapidly rises again to the yield stress. This element continues to undergo plastic strain until failure occurs at about 1.5 milliseconds.

At 3.75 inches from the imperfection site in the axial direction, similar behavior occurs out to 1.5 milliseconds. This position corresponds to gage location B2. This element, however, maintains its ability to carry load because the redistribution of the stress is made over a larger number of elements. A reduction in stress is noted at about 2.1 milliseconds when surface cutoff occurs.

Additional physical understanding can be gleaned from the effective plastic strain plot in Figure 91. The effective plastic strain rate increases as distance to the failure zone decreases. Thus, although the element 3.75 inches from the failure site experienced stress

at the yield value for nearly 1.5 milliseconds, the element did not fail because the plastic strain rate was relatively low. As distance from the failure zone increases the redistributed stress is spread out over a larger area which reduces the plastic strain rate. The plateaus in the near failure zone elements occurred whenever the effective stress dropped below the yield stress.

The initial element failures at 0.4 milliseconds were also reflected in the strain time-history plots. As shown in Figures 84 and 85, the original model and failure model strain predictions are almost identical until 0.4 milliseconds which corresponds to the failure time of the first element. The strain prediction curves diverge after the first failures occurred in the failure model.

The sensitivity of cylinder response to the location of the imperfection zone can be seen in Figure 92. The hoop strain at location E1 was poorly predicted by both the failure model and the original model. The movement of the failure zone one element row or 1.5 inches towards the front of the cylinder resulted in a significant improvement in strain comparisons. Thus, the cylinder response was seen to be sensitive to element thickness reduction, imperfection location and imperfection zone size. In addition, failures which occur in one area of the cylinder can result in a vastly different response at other locations. The failures which occurred at the top of the side-on attack cylinder could have caused the tensile hoop strain noted in Figure 92.
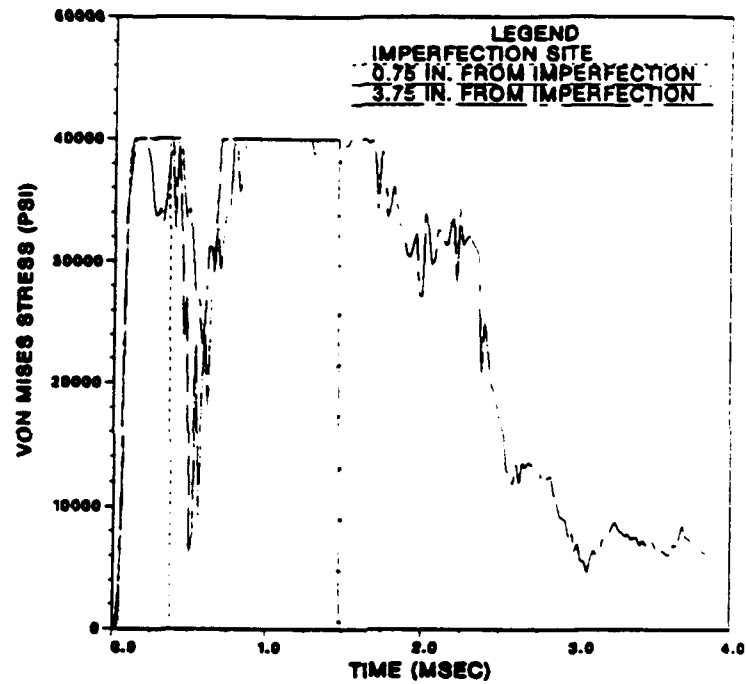
Figure 90. Effective Stress Near Failure Zone Adjacent to Gage Location A2.
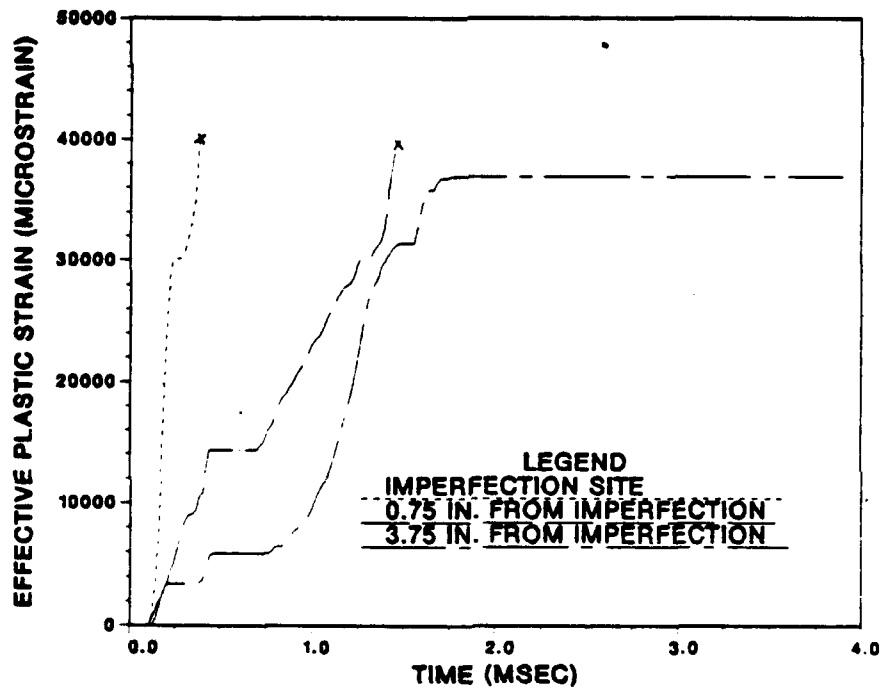
Figure 91. Effective Plastic Strain Near Failure Zone Adjacent to
Gage Location A2.

79
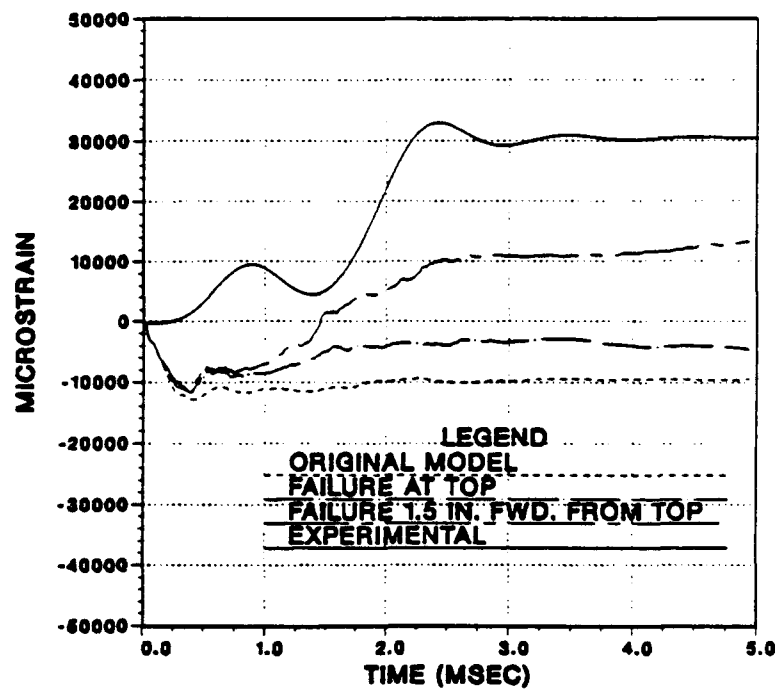
Figure 92. Side-On Explosion Hoop Strain at Gage Location E1 with Different Failure Zone Locations.

V. CONCLUSIONS AND RECOMMENDATIONS

The primary conclusion of this study is that good qualitative strain predictions near a structural failure zone require use of a numerical model which incorporates failure criteria. The significant changes in cylinder response as a direct result of a failure are not well predicted by a numerical model without this criteria.

The use of a ring stiffener in these two cylinders aided in localization of the failure zones and maintenance of the cylindrical geometry. The strain behavior in both cylinders was well predicted remote from the failure zones with numerical models which did not incorporate failure criteria. This was true even in the end-on attack case where the ring stiffener was breached by the propagation of the longitudinal tear.

The simple technique of element thickness reduction to produce failures in a desired location was effective and helpful for understanding the physical nature of dynamic response. This response was very sensitive to the amount of thickness reductions and location of the affected elements.

The presence of imperfection zones in the structure appeared to be a dominant factor in the location and occurrence of cylinder failures. The failure zone near the top of the side-on attack cylinder represented a relatively low strain area yet major failures occurred at this location.

The use of the four node shell element model was the most efficient and accurate model. The additional computational effort required to run a thick shell model would be

better used in construction of a finer shell element mesh. Differences in modeling techniques near the endplate boundaries resulted in fairly significant strain prediction variations near the boundary. These end effects were less significant near the center of the cylinder.

Strain variations due to cylinder rotation from misalignment were minor due to the short range between the charge and cylinder. Greater strain variations due to rotation were seen in the end-on attack cylinder. In both cases, the best numerical strain results occurred at zero degrees rotation.

Mesh density effects were also seen to have a modest effect on numerical strain predictions. The half-cylinder model with 544 elements provided adequate accuracy in all cylinder locations.

Several recommendations should be considered to improve future underwater explosion tests. First, the presence of imperfections and material property variations should be incorporated into future numerical models. Application of random imperfections should be investigated for this purpose. Second, the use of more rugged strain gages designed to withstand greater cyclic fatigue should be considered to avoid the 25% failure rate observed on this test. Finally, further investigation into the use of failure models in the VEC/DYNA3D library should be undertaken to determine the most effective failure model for underwater shock testing.

APPENDIX - HALF-CYLINDER MODEL INGRID INPUT FILE

```
RING-STIFFENED HALF CYLINDER MODEL
dn3d vec term  0.010 plti 20.0e-6 prti 1000.0

mat 1 type 3 e 1.08e+7 pr 0.33 ro 2.610e-4 etan 0.0 sigy 4.0e+4
     shell quad 3 thick 0.25 endmat
     c     material 1 is 0.25 inch thick T-6061 aluminum plate.
     c     material 1 is used in the lateral part of the shell.
     c     Kinematic/Isotropic Elastic/Plastic model.

mat 2 type 3 e 1.08e+7 pr 0.33 ro 2.610e-4 etan 0.0 sigy 4.0e+4
     shell quad 3 thick 1.0 endmat
     c     material 2 is 1.0 inch thick T-6061 aluminum plate.
     c     material 2 is used for the ends of the cylinder.
     c     Kinematic/Isotropic Elastic/Plastic model.

mat 3 type 3 e 1.08e+7 pr 0.33 ro 2.610e-4 etan 0.0 sigy 4.0e+4
     shell quad 3 thick 0.25 endmat
     c     material 3 is the internal ring stiffener

lcd 1 2 0.0  0.0     5.0e-2   0.0
lcd 2 2 0.0  4.0e-7  5.0e-2   4.0e-7

plan 1

0 0 0 1 0 0  0.001 symm

c    define cylindrical surfaces.

c    name    type   point   dir vector   size
     sd 1    cyli   0 0 0    0 1 0         6.0         c  outer shell (circular)
     sd 2    cyli   0 0 0    0 1 0    [6.0*4./6.]  c  inner shell (vertexed)
     sd 3    cyli   0 0 0    0 1 0         5.0         c  inner radius of stiffener

start    c   one quarter inch thick T-6061 aluminum cylinder.

c    part definition.

    -1    3    7   11   -13 ;
     1    6   14   22    27 ;
    -1    3    7   11   -13 ;

    -1. -1.    0.    1.    1.
   -20.5 -12.5  0.0   12.5  20.5
    -1. -1.    0.    1.    1.

pri -1  -5 ; ;-1  -5 ;  1 -1.0  0.0 0.0 0.0

c    deletions for surface formation.

   di 1 2 0 4 5 ; ; 1 2 0 4 5 ;     c   delete corners for surface formation.
   d 2 0 2 4 0 4                     c   delete interior to form shell.

c    surface formation.

   sfi -1 -5 ; ; -1 -5 ; sd 1        c   form cylindrical outer surface.

   d 1  0  0  3  0  0

   mate 1                   c    shell is made of material 1.

end                        c    end part.

start    c  one inch thick T-6061 aluminum positive endplate.
```

83

```
c    part definition.

   1    3    7   11   13 ;              c   element sequence in x-direction.
  -1 ;                                  c   element sequence in y-direction.
   1    3    7   11   13 ;              c   element sequence in z-direction.

  -1.  -1.   0.   1.   1.              c   dimensional info for x-dir elem.
  20.5                                 c   dimensional info for y-dir elem.
  -1.  -1.   0.   1.   1.              c   dimensional info for y-dir elem.

pr 1 1 1 5 1 5     1   -1.0    0.0 0.0 0.0

c    deletions for surface formation.

  di 1 2 0 4 5 ; ; 1 2 0 4 5 ;         c  delete corners for circle formation.

c    surface formation.

  sfi  -1 -5 ; ; -1 -5 ;  sd 1        c   form circular outer shape.
  sfvi -2 -4 ; ; -2 -4 ;  sd 2        c   form vertexed filler for interior.

  d 1  0   0   3   0   0

 mate 2                               c  endplate is made of material 2.

end                                   c  end part.

start    c  one inch thick T-6061 aluminum negative endplate.

c    part definition.

   1    3    7   11   13 ;              c   element sequence in x-direction.
  -1 ;                                  c   element sequence in y-direction.
   1    3    7   11   13 ;              c   element sequence in z-direction.

  -1.  -1.   0.   1.   1.              c   dimensional info for x-dir elem.
 -20.5                                 c    dimensional info for y-dir elem.
  -1.  -1.   0.   1.   1.              c   dimensional info for y-dir elem.

pr 1 1 1 5 1 5     1   -1.0    0.0 0.0 0.0

c    deletions for surface formation.

  di 1 2 0 4 5 ; ; 1 2 0 4 5 ;         c  delete corners for circle formation.

c    surface formation.

  sfi  -1 -5 ; ; -1 -5 ;  sd 1        c   form circular outer shape.
  sfvi -2 -4 ; ; -2 -4 ;  sd 2        c   form vertexed filler for interior.

  d 1  0   0   3   0   0

 mate 2                               c  endplate is made of material 2.

end                                   c  end part.

start    c  one quarter inch thick center stiffener.

c    part definition.

   1    3    7   11   13 ;              c   element sequence in x-direction.
  -1 ;                                  c   element sequence in y-direction.
   1    3    7   11   13 ;              c   element sequence in z-direction.
```

```
   -1.  -1.   0.   1.   1.              c   dimensional info for x-dir elem.
     0.00                                c   dimensional info for y-dir elem.
   -1.  -1.   0.   1.   1.              c   dimensional info for y-dir elem.

c    deletions for surface formation.

  di 1 2 0 4 5 ; ; 1 2 0 4 5 ;        c  delete corners for circle formation.
  d  2 0 2 4 0 4

c    surface formation.

  sfi  -1 -5 ; ; -1 -5 ;  sd 1        c  form circular outer shape.
  sfi  -2 -4 ; ; -2 -4 ;  sd 3        c  form vertexed filler for interior.

  d 1  0  0  3  0  0

 mate 3

end                                   c  end part.

end                                   c  end model.
```

LIST OF REFERENCES

1. Jackson, L.B., *Digital Filters and Signal Processing*, Kluwer Academic Publishers, Boston, Massachusetts, 1986, p. 105-107.

2. Livermore Software Technology Corporation Report 1018, *VEC/DYNA3D User's Manual (Nonlinear Dynamic Analysis of Structures in Three Dimensions)*, by Stillman, D.W., and Hallquist, J.O., June 1990.

3. Livermore Software Technology Corporation Report 1019, *LS-INGRID: A Pre-processor and Three-Dimensional Mesh Generator for the Programs LS-DYNA3D, LS-NIKE3D and TOPAZ-3D, version 3.0,* by Stillman, D.W., and Hallquist, J.O., June 1991.

4. Livermore Software Technology Corporation Report 1009, *LS-TAURUS, An Interactive Post-processor for the Programs LS-DYNA3D, LS-NIKE3D and TOPAZ-3D,* by Hallquist, J.O., April 1990.

5. DeRuntz, J.A. Jr., *The Underwater Shock Analysis Code and its Applications,* Paper presented at the 60th Shock and Vibration Symposium, Virginia Beach, Virginia, 1989.

6. Geers, T.L., "Residual Potential and Approximate Methods for Three Dimensional Fluid-Structure Interaction Problem," *Journal of the Acoustic Society of America,* v. 49, pp. 1505-1510, 1971.

7. Fox, P.K., *Nonlinear Dynamic Response of Cylindrical Shells Subjected to Underwater Side-On Explosions,* Master's Thesis, Naval Postgraduate School, Monterey, California, 1992.

8. Geers, T.L., "Computational Methods for Transient Analysis," *Boundary Element Methods for Transient Response,* Elsevier Science Publishing Co., Inc., New York, New York, p. 231, 1983.

9. Belytschko, T., Lin, J., and Tsay, C.S., "Explicit Algorithms for Nonlinear Dynamics of Shells," *Computational Methods in Applied Mechanical Engineering,* v. 42, pp. 225-251, 1984.

10. Boticario, L.A., *Dynamic Response of Cylindrical Shells to Underwater End-On Explosion,* Master's Thesis, Naval Postgraduate School, Monterey, California, 1991.

11. Livermore Software Technology Corporation Report 1018, *LS-DYNA3D Theoretical Manual,* by Hallquist, J.O., June 1991, p. 123.

INITIAL DISTRIBUTION LIST

No. Copies

1. Defense Technical Information Center 2
   Cameron Station
   Alexandria, Virginia 22304-6145

2. Library, Code 052 2
   Naval Postgraduate School
   Monterey, California 93943-5002

3. Professor Y. W. Kwon, Code ME/Kw 1
   Department of Mechanical Engineering
   Naval Postgraduate School
   Monterey, California 93943

4. Professor Y. S. Shin, Code ME/Sg 1
   Department of Mechanical Engineering
   Naval Postgraduate School
   Monterey, California 93943

5. Department Chairman, Code ME 1
   Department of Mechanical Engineering
   Naval Postgraduate School
   Monterey, California 93943

6. Dr. Thomas T. Tsai 1
   Defense Nuclear Agency
   5801 Telegraph Road
   Alexandria, Virginia 22310

7. Dr. Kent Goering 1
   Defense Nuclear Agency
   6801 Telegraph Road
   Alexandria, Virginia 22310

8. Mr. Douglas Bruder   1
    Defense Nuclear Agency
    6801 Telegraph Road
    Alexandria, Virginia 22310

9. Dr. Phillip B. Abraham   1
    Office of Naval Research
    Mechanics Division, Code 1132
    800 North Quincy Street
    Arlington, Virginia 22217-5000

10. Mr. Gene Remmers, ONT-23   1
    Director, Office of Naval Technology
    800 North Quincy Street
    Arlington, Virginia 22217-5000

11. Professor Thomas L. Geers   1
    Department of Mechanical Engineering
    Campus Box 427
    University of Colorado
    Boulder, Colorado 80309

12. Dr. John A. Deruntz Jr.   1
    Computational Mechanics Section
    Lockheed Palo Alto Research Laboratories
    3251 Hanover Street
    Organization 93-30
    Palo Alto, California 94304

13. Naval Engineering Curricular Office (Code 34)   1
    Naval Postgraduate School
    Monterey, California 93943-5002